Applied Acoustics 212 (2023) 109579

Contents lists available at ScienceDirect

Applied Acoustics

journal homepage: www.elsevier.com/locate/apacoust

Experimental and predicted leading- and trailing-edge noise of symmetric airfoils under zero mean-loading

Laura Botero-Bolívar *, Fernanda L. dos Santos, Cornelis H. Venner, Leandro D. de Santana

University of Twente, Drienerlolaan 5, Enschede, 7522 NB, Netherlands

ARTICLE INFO

Keywords:
Aerodynamic noise
Leading-edge noise
Trailing-edge noise
Amiet's theory
Phased array microphone measurements
Inflow turbulence
Airfoil-rod configuration

ABSTRACT

Incorporating the effect of airfoil geometry in airfoil noise prediction methods is paramount to designing silent wind turbines and achieving regulation limits. However, the airfoil geometry effect on the leading- and trailing-edge noise has not been fully understood. To address this, our research uses a phased microphone array to measure the leading- and trailing-edge noise of airfoils NACA 0012, 00018, 0008, and 63018, which have different chord lengths. The inflow turbulence is generated by a rod located upstream of the airfoils. The far-field noise is compared with Amiet's theory for both noise sources. The results show that the leading-edge noise reduces with the leading-edge radius and maximum thickness in the high- and mid-frequency ranges, respectively. Scaling laws based on these geometric parameters are proposed. The trailing-edge noise of the several airfoils was compared at several velocities and Reynolds numbers. Scaling laws using these quantities were proposed for each case. Furthermore, the competition of leading- and trailing-edge noise mechanisms are assessed when airfoils are subjected to inflow turbulence. The dominant noise source varies in function of the airfoil geometry and frequency. The inflow turbulence increases the trailing-edge noise of the different airfoils. Furthermore, it dominates in a larger frequency range for the thickest airfoil.

1. Introduction

The noise produced by aerodynamic surfaces has become the objective of several research due to its impact on the quality of life of people and wild animals [1–5]. Therefore, stricter regulations have arisen in several fields [6], such as aeronautics [7], underwater applications [8], and wind energy [9], to reduce and maintain low the noise levels. Specifically for wind energy, the noise produced by wind turbines is nowadays the main limitation for installing them closer to urban zones, which have unique favorable conditions capable of boosting the wind turbines' aerodynamic performance [10–12].

The main aerodynamic noise sources of a wind turbine are the leading- and trailing-edge noise [13]. The trailing-edge (TE) noise is caused by the interaction of the turbulent boundary layer with the airfoil surface. This interaction induces wall-pressure fluctuations close to the TE that are scattered to the far field as noise due to the TE discontinuity and the sudden change of impedance [14]. With uniform inflow and an attached turbulent boundary layer, the TE is the unique noise source of an aerodynamic surface. Therefore, it is the minimum amount of noise that an aerodynamic surface can produce, becoming the main noise source of wind turbines [13,15]. On the other hand, when the inflow is turbulent, the inflow turbulence interacts with the airfoil's leading edge (LE), producing high-pressure fluctuations in the airfoil surface, which cause lift fluctuations. This unsteady force production is radiated to the far field as broadband noise, also known as LE noise [16,17]. The inflow turbulence typically has turbulent structures that are significantly larger than those present in a turbulent boundary layer. Thus, LE noise is characteristically a low-frequency noise, whereas the TE noise is characteristically a high-frequency noise [14]. Although both LE and TE noise have been modeled, the influence of the airfoil's geometry in noise production has not been fully understood and incorporated in noise prediction methods and design of wind turbines.

The most common methodology to predict TE and LE noise is Amiet's theory [14,16]. This model was developed for a flat plate where the airfoil geometry is not considered. The input for the TE noise prediction in Amiet's method is the wall-pressure spectrum close to the TE, whereas for the LE noise prediction is the 2D turbulence spectrum upstream of the airfoil LE. Several semiempirical models for the wall-pressure spectrum have been proposed [18–23], which use several

* Corresponding author.
E-mail address: l.boterobolivar@utwente.nl (L. Botero-Bolívar).

https://doi.org/10.1016/j.apacoust.2023.109579
Received 22 February 2023; Received in revised form 2 August 2023; Accepted 6 August 2023
Available online 28 August 2023

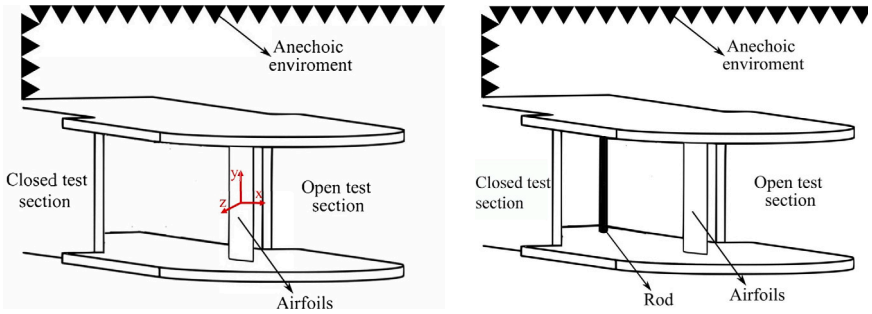

(a) Uniform inflow (b) Turbulent inflow

Fig. 1. Schematic representation of the experimental setup.

boundary layer parameters at the TE as input. Contrary, the method proposed by Blake [24] and Parchen [25], known as TNO-Blake model, consists of obtaining the wall-pressure spectrum by solving the Poisson equation. The model calculates the wall-pressure spectrum by integrating several flow quantities across the boundary layer. This method has been extended by several authors [25–28]. TNO-Blake model is used in this research as input for predicting the TE far-field noise with Amiet's theory. On the other hand, a widely used method for modeling the turbulence spectrum used as input in the LE noise prediction is the von Kármán energy spectrum [29], which uses as input the turbulent integral length scale and the root mean square (rms) of the velocity fluctuations. In this research, the extension of the von Kármán model for correcting the dissipation range proposed by [30] is adopted. Although Amiet's model does not consider the airfoil geometry for any of both noise sources, the airfoil geometry can be considered somehow in the TE noise prediction during the calculation of the boundary layer parameters. However, for the LE noise prediction, the airfoil geometry is not evaluated at any prediction step since the inputs are based on the upstream inflow turbulence. Therefore, it is important to experimentally evaluate the effect of the airfoil geometry on both noise mechanisms and on their competition when the airfoil is subjected to inflow turbulence.

Research has been conducted to evaluate the TE noise produced by a single airfoil [28,31–35]. However, little research compares the TE noise generated by several airfoils. Oerlermans and Migliore [36] compared the TE noise generated by seven different airfoils at several angles of attack and concluded that noise production highly depends on the aerodynamic loading. Therefore, the relative level of the far-field noise spectrum among the airfoils depends on the angle of attack. Contrarily, for LE noise, several research has been conducted to understand the influence of the airfoil geometry. Paterson and Amiet [37] studied experimentally the noise produced by a NACA 0012 at several angles of attack. They found that the angle of attack only causes a slight increase in far-field noise. However, it affects the wall-pressure fluctuations close to the LE, mainly in the high-frequency range. Similar results have been found by [38]. Gershfeld [39] studied the effect of the thickness of the airfoil by creating a single Green's function for each airfoil to predict the far-field noise. They found a reduction of LE noise by increasing the airfoil thickness. Oerlermans and Migliore [36] studied the LE and TE noise of six different airfoils, candidates for small wind turbines, besides a NACA 0012 for comparison with benchmarks. They found that the LE noise increases with the increase in sharpness of the model's LE. Devenport et al. [40] studied the LE noise produced by three different airfoils of different chords, thicknesses, and camber. They found that thicker airfoils generate lower LE noise at high frequencies, but they argued that this effect is not only caused by the LE radius or airfoil thickness. They also found that the camber has a small effect on noise production, whereas the angle of attack has a great effect on the airfoil response function. However, this effect is attenuated by the presence of isotropic turbulence. Gill et al. [41] used computational aeroacoustic methods to systematically study the effect of the LE radius and airfoil thickness by varying those parameters on a baseline symmetric airfoil. They also found that increasing the airfoil LE radius and thickness reduces the LE noise. This reduction effect is more significant for higher frequencies and higher inflow velocities.

This research shows a detailed comparison of the LE and TE noise produced by several airfoils with different chords and thicknesses: 200 mm chord NACA 0012 and 0018, and 300 mm chord NACA 0008, and 63018, which results in two airfoils with the same relative thickness respect to the airfoil chord, and two airfoils with the same absolute thickness. This allows to precisely evaluate the effect of the airfoil thickness and LE radius in the LE noise production along the frequency range. Furthermore, the effect of the Reynolds number for a given inflow velocity in the TE noise can be evaluated because of the different airfoils' chord lengths. Therefore, this research presents several scaling laws that would help to further compare and predict LE and TE noise of different airfoils. The analyses also include comparisons of the measured 1D inflow turbulence spectrum with the von Kármán spectrum and the measured wall-pressure spectrum with the TNO-Blake model. The far-field noise of both noise sources are compared with Amiet's theory. Moreover, this research compares, for the first time, the noise produced by a single airfoil with and without inflow turbulence to analyze the competition between LE and TE noise mechanisms as a function of the frequency and airfoil geometry. The remaining part of this paper is organized as follows. Section 2 shows the experimental methodology. Section 3 presents the noise prediction methods. Section 4 discusses the LE and TE noise of every airfoil and the comparison of each noise source among the airfoils. Section 5 addresses the comparison of the noise produced by a single airfoil with and without inflow turbulence for the NACA 0008 and 63018. Finally, Sec. 6 presents the conclusions of the study.

2. Experimental methodology

Experiments consisted of acoustic measurements with a phased microphone array of four different airfoils with and without inflow turbulence. The inflow turbulence is generated by a rod located upstream of the airfoils' LE. Fig. 1 shows a schematic representation of the experimental setup for both inflow conditions. The coordinate reference system is x in the streamwise direction, y in the spanwise direction, and z normal to the airfoil wall. The origin of the coordinated system is at midchord and midspan, which is coincident for all the airfoils.

2.1. Wind tunnel

Experiments were conducted in the open jet configuration of the Aeroacoustics wind tunnel of the University of Twente. The facility is a closed-circuit wind tunnel that allows measurements in an open test section, closed test section, and hybrid test section [42]. It has seven turbulence screens followed by a contraction rate of 10:1 that keep the

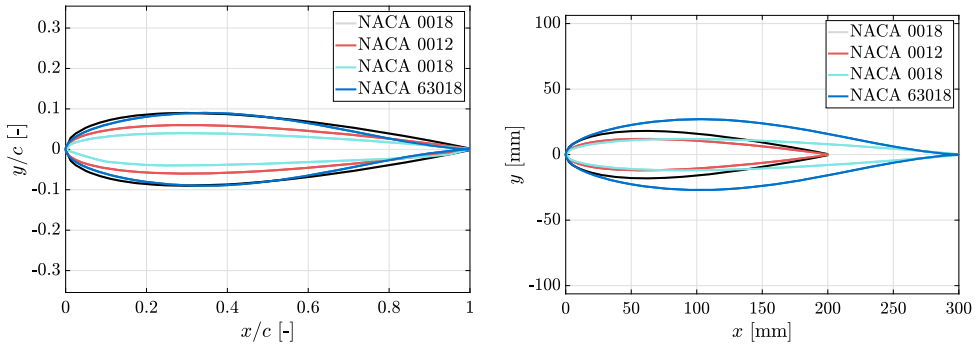

(a) Scaled by the airfoil chord (b) Non-scaled

Fig. 2. Airfoils' geometry.

Table 1
Airfoils' geometric characteristics.

Airfoil	c [mm]	t [mm]	a [mm]
NACA 0018	200	36	7.1
NACA 0012	200	24	3.2
NACA 0008	300	24	2.1
NACA 63018	300	54	6.36

turbulence level below 0.08% in the open test section at the maximum operating velocity of 60 m/s [43]. The test section is 0.7 m height and 0.9 m width and is inside an anechoic chamber with an empty cut-off frequency of 160 Hz. The temperature in the test section is controlled at approximately 20 °C. The airfoils were installed vertically in the section using two rotatory end plates.

2.2. Airfoil models and instrumentation

The airfoils used in this study are NACA 0008, NACA 0012, NACA 0018, and NACA 63018. The NACA 0018 and NACA 0012 have 200 mm chord (c), whereas the NACA 0008 and NACA 63018 have 300 mm chord. Fig. 2 shows the airfoils' coordinates scaled by the chord and non-scaled by chord. Note that the NACA 0018 and 63018 have the same thickness with respect to the airfoil chord (see Fig. 2 (a)), i.e., 18%; however, the absolute thickness is different for both airfoils. Oppositely, the NACA 0012 and 0008 have different thicknesses with respect to the airfoil chord but the same absolute value (see Fig. 2 (b)), i.e., 24 mm. Table 1 shows the LE radius (a) and the maximum thickness (t) of the four airfoils.

The NACA 0018 and NACA 0012 are instrumented with six Knowles FG 23329-P07 microphones under a 0.5 mm pinhole. The microphones are distributed in two rows of three spanwise microphones. The microphone data shown in this research is of the one at x/c=0.4275 and y/c=0. The NACA 0008 and NACA 63018 are instrumented by 82 remote microphone probes located along the span and chord. See refs. [31,44,45] to obtain more information about this technique. The remote microphone probes consist of a pinhole of 0.3 mm connected to a stainless steel tube of 1.5 mm inner diameter that is connected to a PMMA tube assembly, where Knowles FG 23329-P07 microphones and the anechoic termination are connected with the stainless steel tube coming from the airfoil surface. The microphone data shown in this research is of the one at x/c=0.97 and y/c=0.

The microphones under a pinhole and the remote microphone probes were calibrated using an in-house calibrator, which is equipped with a reference microphone, i.e., a GRAS 40HP, and an FR8 loudspeaker that produces white noise as a noise source for the calibration procedure. The calibration consisted of two steps to reduce the influence of the calibrator in the transfer function. A detailed explanation of the calibration procedure can be found in [46].

2.3. Noise measurements

Noise measurements were conducted using a microphone array of 62 GRAS 40PH microphones. The microphone array is a vogel spiral of 1 m diameter. This geometry yields a flat main-lobe-to-sidelobe ratio (MSR) in a wide frequency range [47]. Fig. 3 left shows the microphone array with respect to the airfoils. In the figure, the airfoil chord is 300 mm. For the airfoils with a 200 mm chord, the location of the center is the same; this means that the LE and TE are located 50 mm closer to the x=0. The center of the microphone array was aligned with the center of the airfoils in the same plane as the one composed of the airfoil chord-span lines at a zero angle of attack. The microphone array is at z=1.5 m. The microphones signal was acquired for 30 s at a sampling frequency of 2^{16} (65,536) Hz using PXIe-4499 Sound and Vibration modules installed in a NI PXIe-1073 chassis. The sensitivity of each GRAS 40HP microphone was calibrated using a pistonphone GRAS 42AG Multifunction Sound Calibrator with a sound pressure level of 94 dB and frequency of 1 kHz.

The noise source localization was conducted using the beamforming technique. The in-house algorithm of the technique was benchmarked against an array benchmark database [48,47]. More information about the beamforming methodology and the in-house algorithm can be found in [49]. The cross-spectral matrix (CSM) was calculated adopting the Welch method, with 50% overlap and a window size of 2^{13}, which results in a frequency resolution of 8 Hz. The diagonal of the CSM was removed to avoid contamination of the self-noise of the microphones. No weighting of the microphones was applied. The frequency response calibration provided by the manufacturer was accounted for during the CSM calculation. The search grid for the beamforming was $x \in [-0.5, 0.5]$ m and $y \in [-0.5,\ 0.5]$ m. The grid resolution was 30 mm in both directions.

The quantification of the LE and TE noise was conducted using the source power integration (SPI) technique [50]. The far-field noise spectrum was calculated at the microphone array's center. Therefore, only one directivity angle is analyzed in this study. The region of interest (ROI) for the LE noise evaluation was $x/c \in [-1,\ 0]$ and $y/d \in [-0.3,\ 0.3]$, and the ROI for the TE noise was $x/c \in [0,\ 1]$ and $y/d \in [-0.3,\ 0.3]$. Note that the ROI changes for the different airfoil chords. However, it was confirmed that the different ROI sizes yield similar far-field noise spectra. Fig. 3 right shows both regions of interest, together with the lateral view of the airfoil and wind tunnel walls.

2.4. Wall-pressure spectrum

Unsteady wall-pressure measurements were conducted under the same inflow conditions as the TE noise measurements. The surface microphones were connected to a PXIe-4499 Sound and Vibration modules installed in a NI PXIe-1073 chassis, which acquired the measurements during 30 s in a 2^{16} (65,536) Hz sampling frequency. The wall-pressure

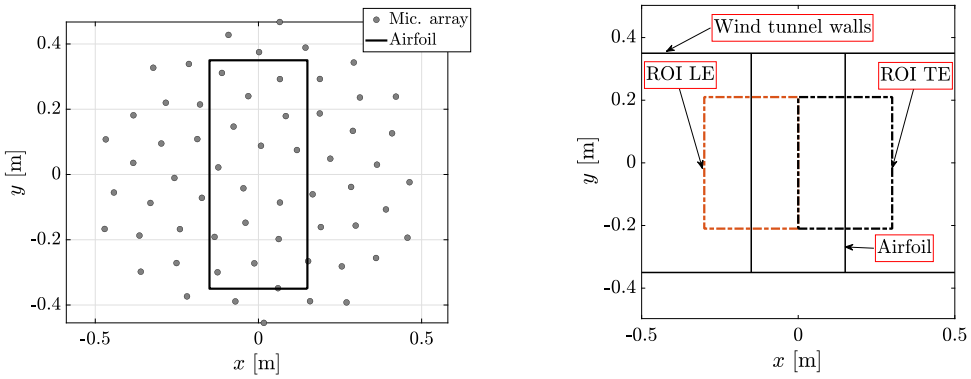

Fig. 3. Left: microphone array. Right: Region of interest for LE and TE noise.

Table 2
Inflow turbulence characteristics at the plane of the airfoil LE without the airfoil installed for the NACA 0012 and 0018 airfoils.

U_∞ [m/s]	Re [-]	u_{rms} [m/s]	L [mm]
15.6	2.0×10^5	3.08	60.0
20.0	2.6×10^5	3.81	68.9
24.0	3.3×10^5	4.55	72.9
32.0	4.0×10^5	5.87	90.5
36.1	4.6×10^5	6.49	92.2
39.3	5.3×10^5	7.13	101

Table 3
Inflow turbulence characteristics at the plane of the airfoil LE without the airfoil installed for the NACA 63018 and 0008 airfoils.

U_∞ [m/s]	Re [-]	u_{rms} [m/s]	L [mm]
15.3	3.0×10^5	1.91	47.1
21	4.0×10^5	2.68	49.4
24.4	5.0×10^5	3.05	50.8
31.1	6.0×10^5	3.65	53.4
34.8	7.0×10^5	3.82	54.9
39.43	8.0×10^5	4.53	56.8

spectrum is calculated using the Welch method with 50% overlap and a window size of 2^{13}, which results in a frequency resolution of 8 Hz.

2.5. Test conditions

2.5.1. Leading-edge noise measurements

The inflow turbulence was generated by a 40 mm diameter rod, installed at the end of the closed test section, see Fig. 1(b), i.e., 685 mm upstream of the LE of the NACA 0018 and 0012 and 635 mm upstream of the LE of the NACA 0008 and 63018. The turbulence generated by the wake of the rod was characterized by hot-wire anemometry measurements without the airfoils installed in the wind tunnel, see ref. [51] for information about the hot-wire measurements methodology. The wake of the rod at the plane of the airfoils' LE was larger than 480 mm. Therefore, every airfoil was inside the rod's wake. The inflow velocity varied from 15 to 45 m/s with increments of 5 m/s. No tripping devices were installed on the airfoil surface.

Tables 2 and 3 show the inflow turbulence parameters for each pair of airfoils, where U_∞ is the inflow velocity, Re is the Reynolds number calculated based on the airfoil chord, u_{rms} is the rms of the velocity fluctuations, and L is the turbulent integral length scale in the streamwise direction. L is calculated following the methodology proposed by Hinze [52], which adopts the Taylor's hypothesis of frozen turbulence [53]. The turbulent time scale (τ) corresponds to the integration of the normalized autocorrelation of the velocity time-history from zero up to the first-zero crossing and $L = U\tau$. The turbulence intensity and integral length scale at the LE's plane vary slightly for the NACA 0012 and 0018 and for the NACA 0008 and 63018. However, the integral length scale is significantly larger than the LE radii and small than the airfoil chord in all the cases. Therefore, we expect the LE noise phenomenon to be similar for each case. The turbulence characteristics shown in Tables 2 and 3 are used to scale the LE noise produced by the different airfoils and to calculate the 1- and 2-D von Kármán spectrum.

2.5.2. Trailing-edge noise measurements

The TE noise was measured under the low-turbulence uniform inflow generated by the wind tunnel. The inflow velocity varied from 20 to 40 m/s with increments of 10 m/s. The boundary layer transition was forced at 5% of the airfoil chord by using tripping devices. The tripping device consists of a zigzag strip of 60° top angle and 12 mm width. The tripping device height (k) was varied among the airfoils and velocities to keep a roughly constant $k/\delta_k \approx 0.6$ among the different conditions, following the recommendations of ref. [54], where δ_k is the boundary layer thickness at the trip location. δ_k is obtained as explained in Sec. 3.2.2.

3. Far-field noise prediction methods

LE and TE noise are predicted using Amiet's theory. The theory assumes a flat plate geometry with an infinitely small thickness, a stationary observer, and a uniform free-stream condition along the span. The model calculates the far-field power spectral density of a flat plate of chord c and span d. In LE and TE formulations, k ($= \omega/c_0$) is the acoustics wavenumber, and k_x ($= \omega/U_\infty$) and k_y are the chordwise and spanwise hydrodynamics wavenumbers, respectively. σ^2 ($= x_o^2 + (1-M^2)(y_o^2 + z_o^2)$) is the flow corrected radial distance, where M is the Mach number, and x_o, y_o, and z_o are the coordinates of the observer location. As the aspect ratio of the wind tunnel models is significantly small ($= 1.4$ considering the span as the length of the ROI used in the source power integration), the contribution of the spanwise wavenumber (k_y) is also considered. Furthermore, the power spectral density calculated by Amiet's theory is, by definition, a double side spectrum (S_{pp}). Therefore, the level needs to be multiplied by a factor of 2. To obtain the one-side spectrum in function of the frequency (G_{pp}), Eq. (1) is used.

$$G_{pp}(x_o, y_o, z_o, f) = (2\times 2\pi) S_{pp}(x_o, y_o, z_o, \omega). \tag{1}$$

The following sections explain the LE and TE noise prediction methods and the obtention of the input parameters.

3.1. Leading-edge noise

Equation (2) shows the power spectral density of the far-field LE noise at the midchord and midspan [16], where $\Phi_{ww}(k_x, k_y)$ is the

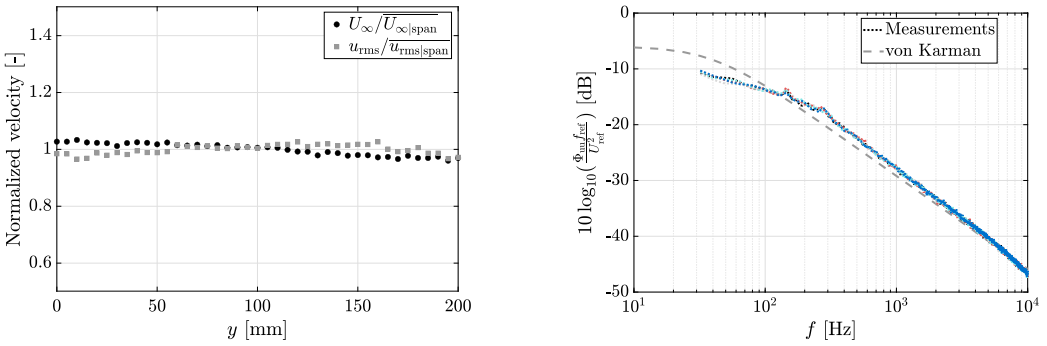

(a) velocity and velocity fluctuations (b) Power spectral density of the velocity spectrum

Fig. 4. Streamwise turbulence characteristics along the height of the wind tunnel in the plane of the leading edge of airfoils NACA 63018 and 0008. U_∞=25 m/s. y=0 is the center of the wind tunnel.

2D perpendicular-to-the-wall velocity spectrum and $\mathscr{L}(x,k_x,k_y)$ is the aeroacoustic transfer function for subcritical or supercritical gusts. $\mathscr{L}$ accounts for the scattering effect of the LE and back-scattering of the TE, implemented with the conclusions of Bresciani et al. [55, Eqs. A1-A4]. The far-field noise is calculated at the reference point used in the source power integration technique. The coordinate reference system in Amiet's theory for LE is located at midchord and midspan. Therefore, the observer location for comparison with wind tunnel experiments is $x_o = y_o = 0$ and $z_o = 1.5$ m.

$$S_{pp} = \left(\frac{\omega z_o \rho c}{2c_o\sigma^2}\right)^2 \pi U_\infty (d/2)\times \int_{-\infty}^{\infty} \left|\mathscr{L}(x_o,k_x,k_y)\right|^2 \Phi_{ww}(k_x,k_y)\frac{\sin^2\left((ky_o/\sigma - k_y)d/2\right)}{\pi(d/2)\left(ky_0/\sigma - k_y\right)^2}\mathrm{d}k_y. \quad (2)$$

3.1.1. Inflow turbulence spectrum

The far-field noise is calculated using the von Kármán inflow turbulence spectrum with the correction for the dissipation range proposed by dos Santos et al. [30, pp. 3586], see Eq. (3), where k_e is the wavenumber scale of the largest eddies [56], calculated as shown in Eq. (4), where L is the integral length scale of the inflow turbulence, which values are shown in Tables 2 and 3, Γ is the gamma function, $B = 4.6$, $n = 1.5$, and η is the Kolmogorov length scale, calculated as shown by [30, Eqs. 14-16].

$$\Phi_{ww}^{\text{vK}}(k_x,0) = \frac{4}{9\pi}\frac{u_{\text{rms}}^2}{k_e^2}\frac{(k_x/k_e)^2}{[1+(k_x/k_e)^2]^{7/3}}\exp(-B(k_x\,\eta)^n). \quad (3)$$

$$k_{\text{e}} = \frac{\sqrt{\pi}}{L}\frac{\Gamma(5/6)}{\Gamma(1/3)}. \quad (4)$$

3.2. Trailing-edge noise

Equation (5) shows the power spectral density of the TE noise using Amiet's theory. In addition to the assumptions discussed at the beginning of this chapter, for the TE noise formulation, the turbulence is assumed to be frozen at the TE discontinuity. $\mathscr{L}$ is modeled for the subcritical and supercritical gust and accounts for the scattering caused by the TE and the back-scattering caused by the presence of the LE. The formulation used in this research follows the one of Roger and Moreau [57]. Amiet's theory assumes that the origin of the coordinate system is at the TE location. Therefore, for the noise to be calculated at the microphone array center, the observer position is $x_o = -c/2$ m, $y_o = 0$ m, and $z_o = 1.5$ m.

$$S_{\text{pp}}(x_o, y_o = 0, z_o, \omega) = \left(\frac{\omega z_o b d}{2\pi c_o \sigma^2}\right)^2 \frac{1}{2\pi c}\times \int_{-\infty}^{\infty} \left|\mathscr{L}\left(bk_x, bk_y\right)\right|^2 l_y(k_y,\omega)\Phi_{\text{pp}}(\omega)\frac{\sin^2\left[\frac{d}{c}(bk_y - bk\frac{y_o}{\sigma})\right]}{\left[\frac{d}{c}(bk_y - bk\frac{y_o}{\sigma})\right]^2}\mathrm{d}(bk_y). \quad (5)$$

In Eq. (5), Φ_{pp} is the wall-pressure spectrum, l_y is the spanwise correlation length and b is the semichord used to nondimensionalize the wavenumbers. The spanwise correlation length is calculated as proposed by Corcos, shown in Eq. (6), where U_c is the convection velocity, assumed as $0.7U$, and b_c is the Corcos' constant equal to 1.47 [28].

$$l_y(k_y,\omega) = \frac{b_c U_c \omega}{b_c U_c k_y^2 + \omega^2}. \quad (6)$$

3.2.1. Wall-pressure spectrum

The wall-pressure spectrum is calculated by adopting the TNO-Blake model. This model is based on the solution of Poisson's equation that results from the divergence of the Navier-Stokes equation simplified by the continuity equation. The model can be applied to calculate the wall-pressure spectrum close to the trailing edge. However, the turbulence quantities are calculated assuming that the discontinuity of the trailing edge does not affect the turbulence. Furthermore, the model assumes that the turbulent pressure and velocity fields are spatially homogeneous and stationary on time. The wall pressure spectrum can be calculated in the wavenumber-frequency domain by applying the time-space Fourier transform. Therefore, the wall pressure spectrum would depend on the wavenumber in the chordwise and spanwise directions. Integration over k_y can be conducted by introducing the spanwise correlation length that depends on the frequency ($l_y(0,\omega)$). In this research, we follow the model extension proposed by Stalnov et al. [28], which also considers the anisotropy of turbulence by incorporating the stretching parameters. The single-point wall pressure spectrum is then calculated as shown in Eq. (7), where δ is the boundary layer thickness; $\Lambda_{z|ww}(z)$ is the turbulent integral length scale across the boundary layer in the z direction, i.e., in the direction across the boundary layer, perpendicular to the airfoil wall; $U_c(z)$ is the convection velocity across the boundary layer; $U(z)$ is the streamwise mean velocity across the boundary layer; $u_{\text{rms,z}}(z)$ is the velocity fluctuations in the z-direction across the boundary layer; and $\phi_{ww}(k_x,z)$ is the spectrum of the velocity fluctuations in the z-direction. See ref. [28, Eqs. 26-37] to obtain information about the modeling of each quantity. The inputs for the modeling of Φ_{pp}, i.e., δ, u_τ, and dp/dx are obtained from XFOIL simulations, explained in Sec. 3.2.2.

$$\Phi_{\text{pp}}(\omega) = \frac{4\pi\rho^2}{l_y(\omega)}\int_0^{\delta}\Lambda_{z|ww}(z)U_c(z)\left[\frac{\partial U(z)}{\partial z}\right]^2\frac{u_{\text{rms,z}}(z)}{U_c^2(z)}\phi_{\text{ww}}(k_x,z)e^{-2k_x z}dz. \quad (7)$$

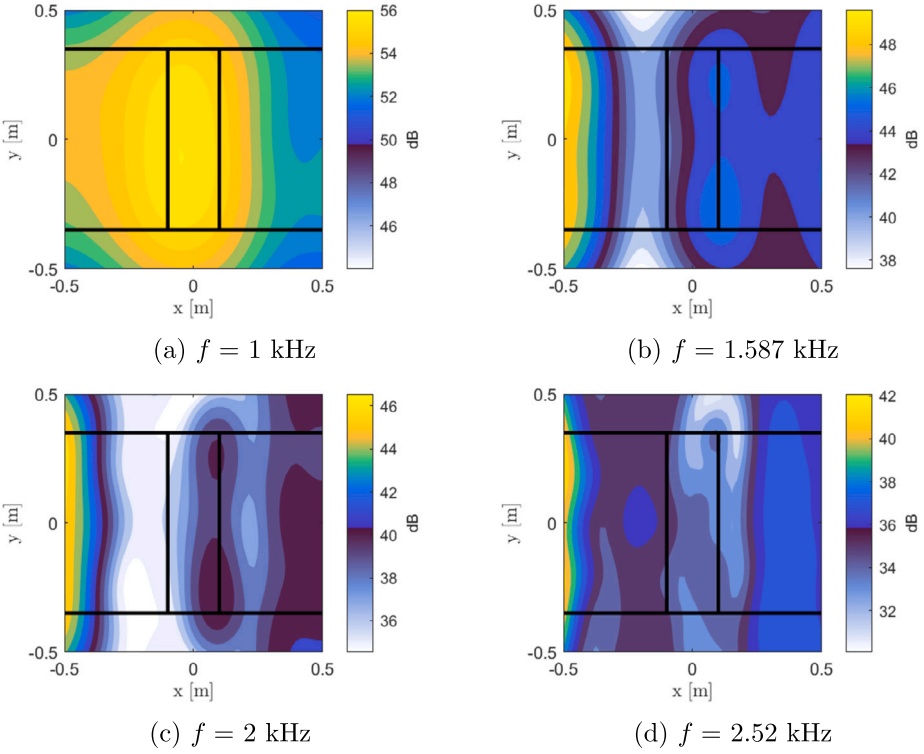

Fig. 5. Beamforming maps with inflow turbulence for NACA 0018 airfoil. U_∞=25 m/s.

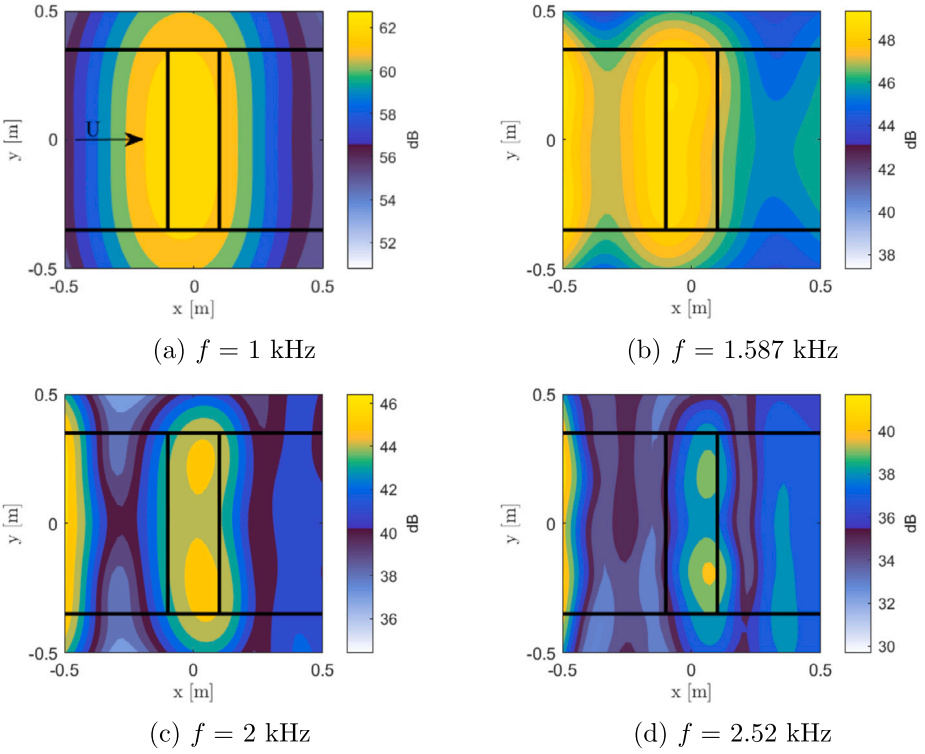

Fig. 6. Beamforming maps with inflow turbulence for NACA 0012 airfoil. U_∞=25 m/s.

3.2.2. *XFOIL simulations*

XFOIL simulations [58] were conducted to obtain the boundary layer thickness at the tripping location to determine the trip height and close to the TE to scale the TE noise and calculate the wall-pressure spectrum using TNO-Blake model explained in Sec. 3.2.1. Previous research has demonstrated the accuracy of XFOIL to determine the boundary layer parameters [28,54]. The input parameters for XFOIL were the airfoil coordinates, the Reynolds number, calculated based on the airfoil chord and inflow velocity, the critical number (N=8.68), and the location of the transition, i.e., 1 for the cases of natural transition and

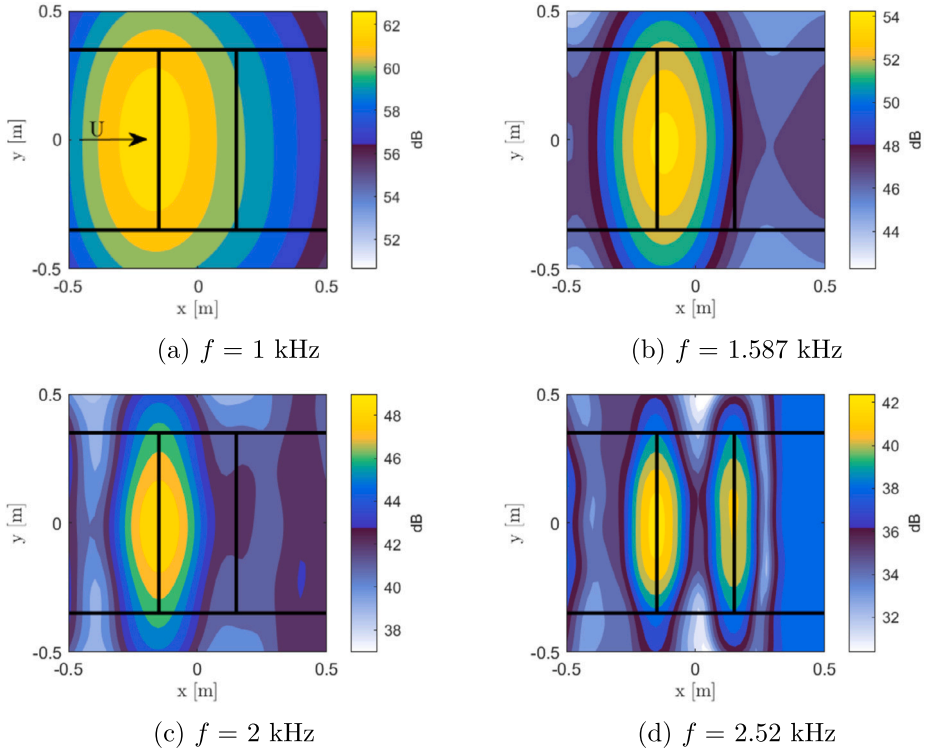

Fig. 7. Beamforming maps with inflow turbulence for NACA 0008 airfoil. U_∞=25 m/s.

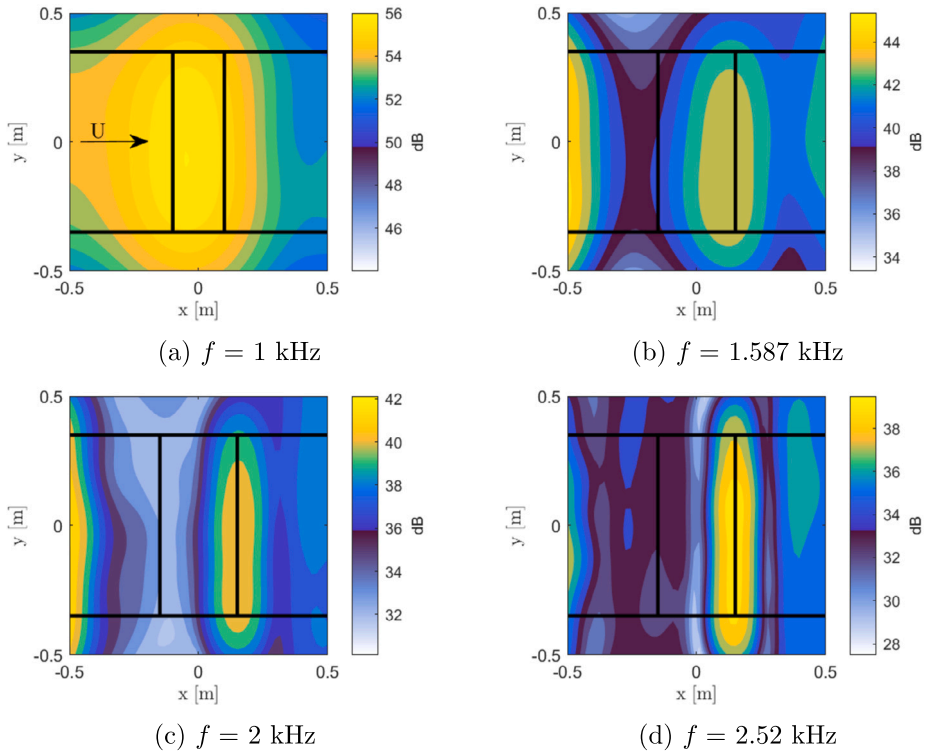

Fig. 8. Beamforming maps with inflow turbulence for NACA 63018 airfoil. U_∞=25 m/s.

0.05 for the cases of forced transition. The natural transition was considered to determine the boundary layer thickness at the trip location (δ_k).

XFOIL computed the boundary layer displacement thickness (δ^*), momentum thickness (θ), and skin friction coefficient (C_f) along the chord. The boundary layer thickness at the trailing edge (δ) and at the trip location (δ_k) was calculated as Eq. (8) [58], where $H = \delta^*/\theta$. The friction velocity (u_τ) is calculated as shown in Eq. (9).

$$\delta = \theta\left(3.15 + \frac{1.72}{H-1}\right) + \delta^*. \tag{8}$$

$$u_\tau = \sqrt{0.5 U_\infty^2 C_f}. \tag{9}$$

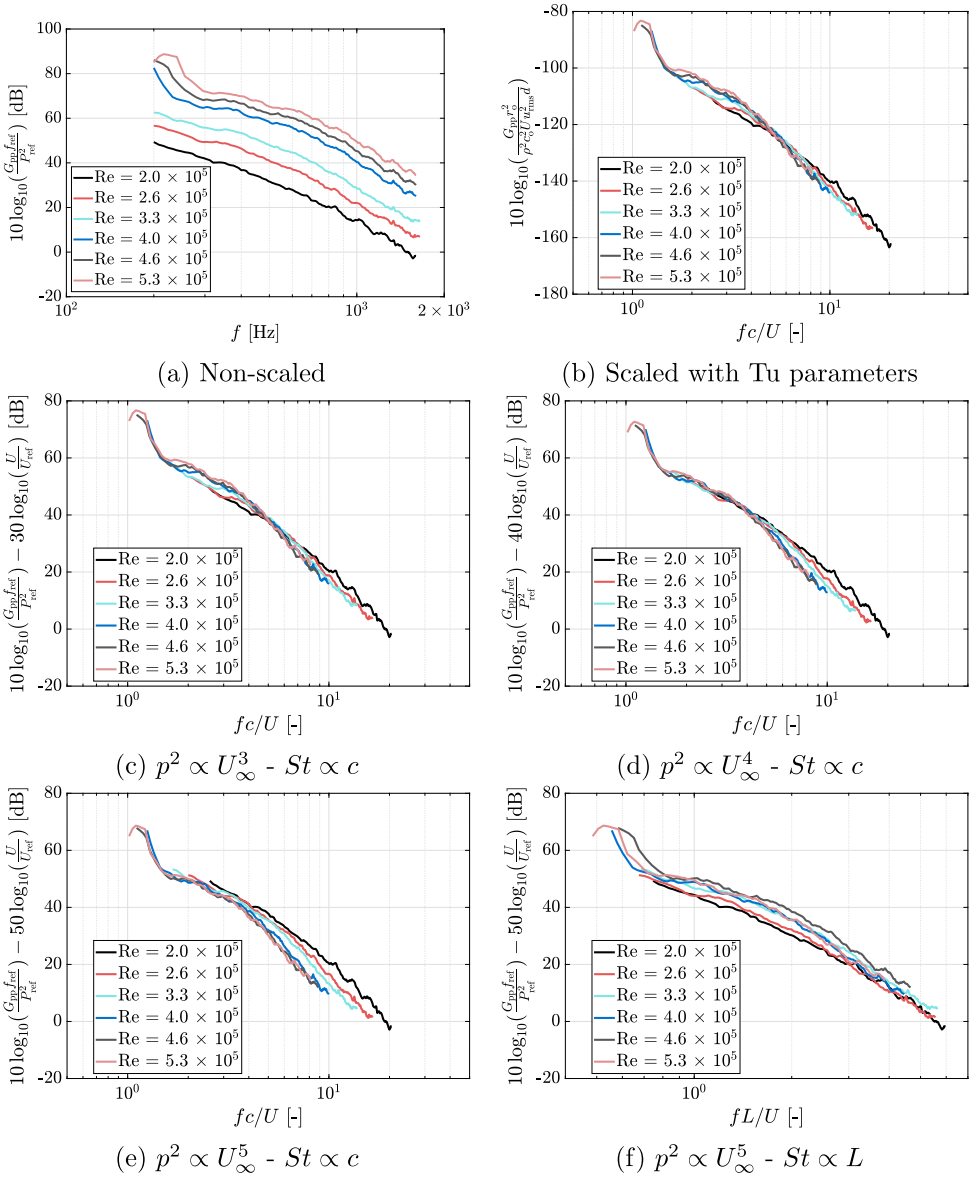

Fig. 9. LE noise for several Reynolds numbers of NACA 0018 airfoil.

Table 4
Boundary layer thickness in mm for the different airfoils at different Reynolds number at $x/c = 0.99$ obtained with XFOIL simulations.

Airfoil \ U [m/s]	20	30	40
NACA 0018	7.9	7.3	7.0
NACA 0012	6.6	6.1	5.8
NACA 0008	8.0	7.4	7.1
NACA 63018	11.7	10.9	10.4

Table 4 shows the boundary layer thickness at the TE ($x/c = 0.99$) for the different airfoils for different inflow velocities. Note that the same inflow velocity corresponds to different Reynolds numbers depending on the airfoil.

4. Leading- and trailing-edge noise of the several airfoils

This section is divided into LE noise and TE noise. First, the comparison between the measured turbulence spectrum and the 1-D von Kármán spectrum and the comparison between the measured wall-pressure spectrum and the TNO-Blake model is presented at the beginning of the LE and TE noise sections respectively. Next, for both noise sources, the beamforming maps are shown for a single inflow velocity; followed by the far-field noise spectrum for each of the four airfoils for several Reynolds numbers and for frequencies where the background noise is at least 4 dB lower than the airfoil noise. Finally, the LE and TE noise produced by the different airfoils are compared in each section.

4.1. Leading-edge noise

4.1.1. Inflow turbulence

The input for the prediction of the LE noise is ϕ_{ww}, which is modeled by the von Kármán model. This quantity was not measured during wind tunnel experiments; only the streamwise velocity was measured. Thus, the one-dimensional von Kármán spectrum is compared with the hot-wire measurements. Fig. 4 shows the power spectral density (PSD) of the streamwise velocity measured at the location where the airfoil leading-edge would be at several locations along the spanwise direction spaced by 50 mm. The experimental velocity spectrum does not show differences for the several spanwise locations, which shows the unifor-

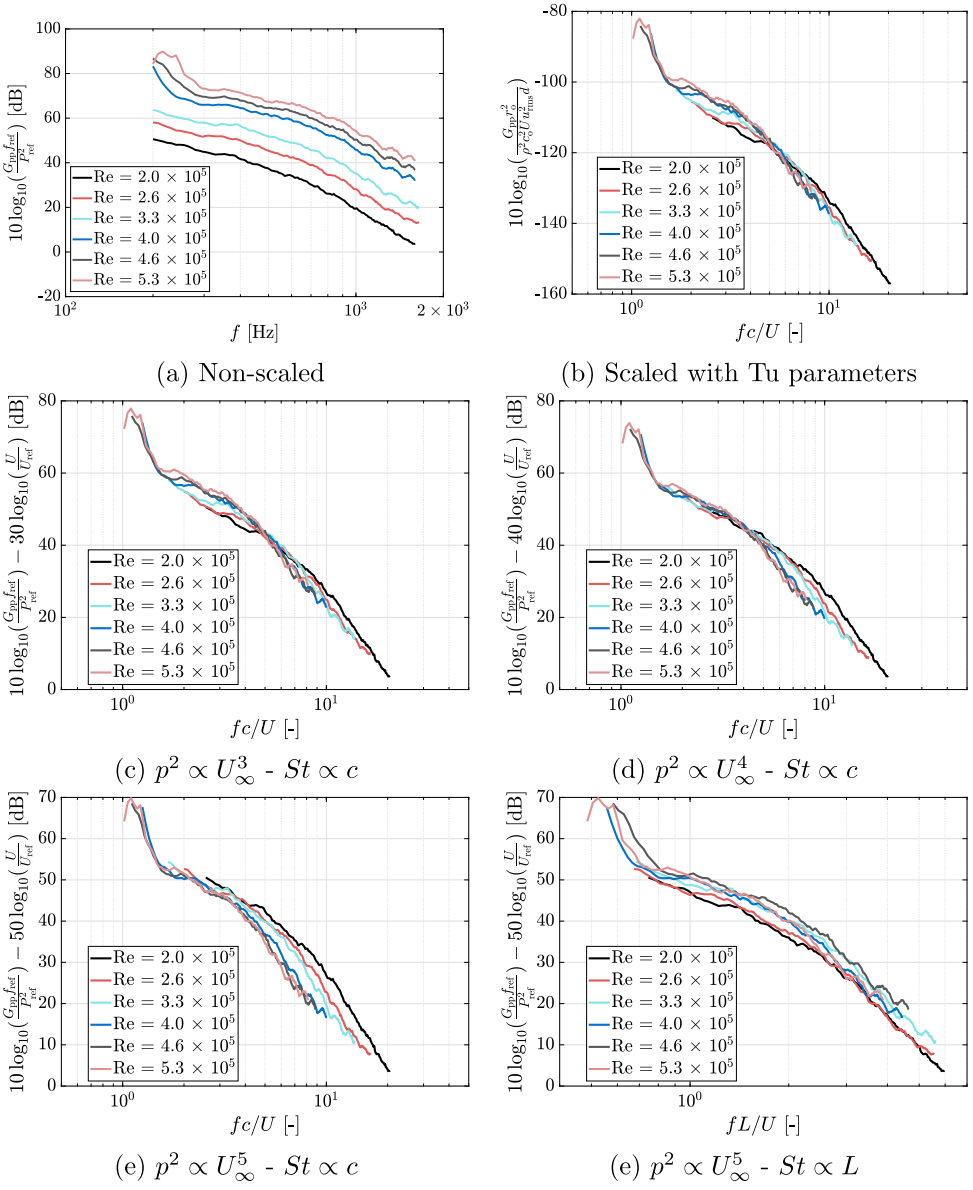

Fig. 10. LE noise for several Reynolds numbers of NACA 0012 airfoil.

mity of the flow. Furthermore, the von Kármán spectrum agrees well with the experimental measurements, mainly for high frequencies. For lower frequencies, the experimental spectrum does not properly follow the von Kármán model, probably because of the large turbulent structures formed in the rod wake caused by the vortex shedding. As the turbulence is generated by the wake of a rod, it probably is not isotropic, and by comparing only the streamwise velocity spectrum ϕ_{uu} with the von Kármán model we are not considering this anisotropy. Nevertheless, even though the von Kármán model was developed for isotropic and homogeneous turbulence; this model can represent well even non-homogeneous flows [59–62]. Therefore, reasonable good estimations of leading-edge noise should be obtained by using the 2-D von Kármán spectrum of ϕ_{ww}. In the literature, comparisons of the ϕ_{uu} with the von Kármán spectrum are shown while the 2-D ϕ_{ww} von Kármán spectrum is used for leading-edge noise prediction with Amiet's theory for grid-generated turbulence, justified by the difficulty of measuring the ϕ_{ww} component to compare with the von Kármán model [31,63,64].

Fig. 4(b) shows the variation of the inflow velocity and the velocity fluctuations normalized by the mean value along the span. The results show that the flow is uniform along the span since variations of less than 3% were found in both inflow velocity and velocity fluctuations. The results are shown for the NACA 0012 and 00018 at U_∞=25 m/s. However, similar uniformity is found for other velocities and for the NACA 63018 and 0008.

4.1.2. Beamforming maps

Figs. 5, 6, 7, and 8 show the one-third octave beamforming maps for four different central frequencies for the NACA 0018, NACA 0012, NACA 0008, and NACA 63018, respectively, when the rod is installed. The maps are shown only for U_∞=25 m/s for conciseness, but similar results are obtained for other velocities. The flow is coming from left to right in the beamforming maps. In most cases, clear noise sources are observed, indicating that there are no spurious noise sources, such as the interaction of the airfoil with the wind tunnel walls. However, for the NACA 0018 for $f \geq$1.587 kHz, a noise source upstream of the airfoil is observed, see Fig. 5(b,c,d), which is mainly caused by the presence of the rod and the interaction of the flow with the end of the closed test section.

The NACA 0008 (Fig. 7) shows a localized noise source at the LE up to f=2.52 kHz. This airfoil produces LE noise up to the highest

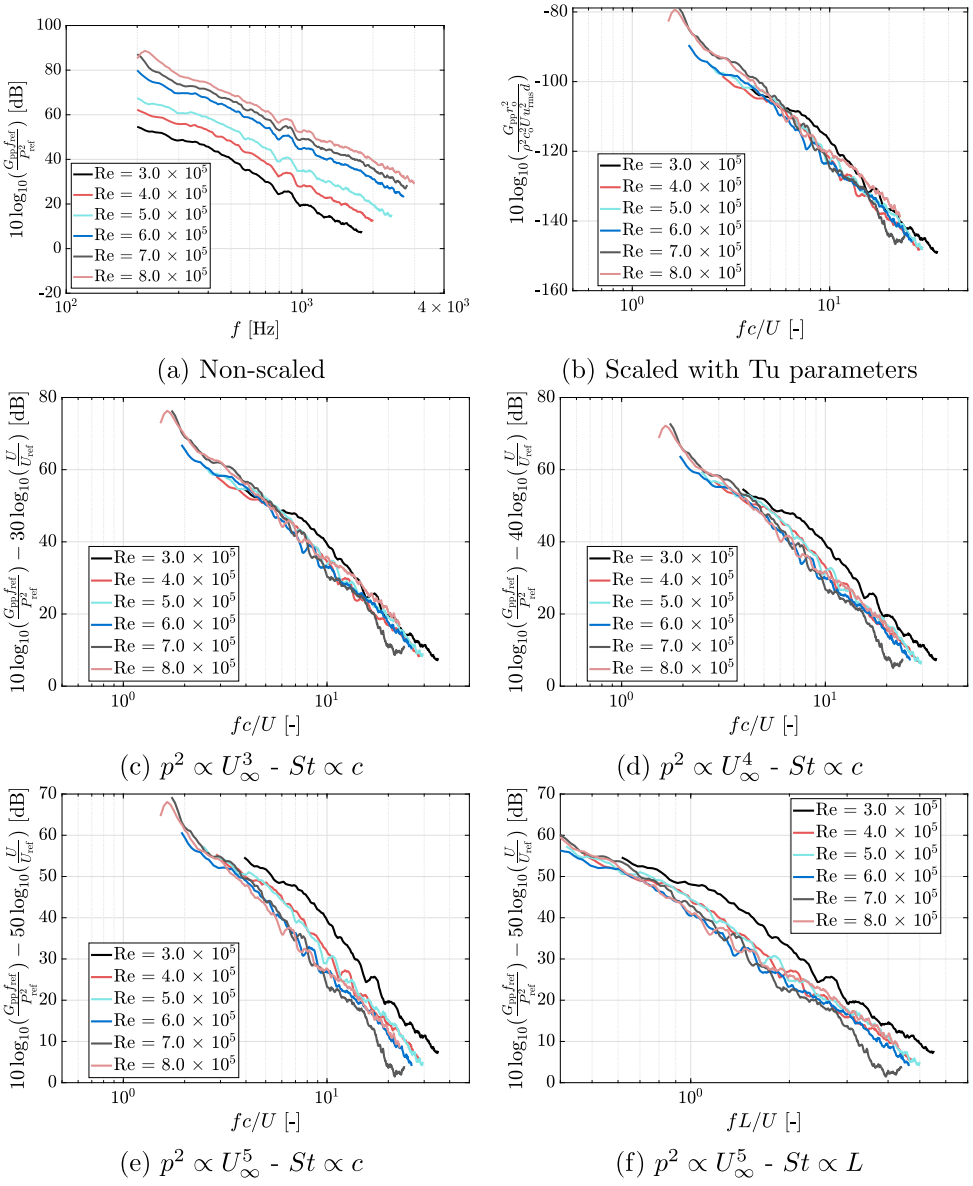

Fig. 11. LE noise for several Reynolds numbers of NACA 0008 airfoil.

frequency among all airfoils. At f=2.52 kHz, the beamforming maps also show a noise source at the TE, with a slightly lower intensity than LE noise. For the NACA 0012 (Fig. 6), a localized noise source at the LE is observed up to f=1.587 kHz. At f=2 kHz, the noise source is shifted downstream along the airfoil chord, and at f=2.52 kHz, a weak noise source is observed at the TE location. For the NACA 63018 (Fig. 8) a noise source at the LE is observed at f=1 kHz and at f=0.5 kHz (not shown here for simplicity). For f>1 kHz, the noise source is mostly located at the TE. This behavior could be explained by two reasons: I. The LE noise produced by the airfoil NACA 63018 is dominant for frequencies lower than 0.5 kHz and the microphone array used in this research is not able to measure and localize the noise source for such low frequencies. II. Even when subjected to inflow turbulence, thick airfoils generate TE noise that is still dominant for a large frequency range, including low frequencies. This phenomenon will be discussed in detail in Sec. 5. A similar behavior is observed for the NACA 0018 (Fig. 5). A noise source located towards the LE is observed at f=1 kHz; however, for f>1 kHz no strong localized noise source is observed, and only a weak noise source appears at the TE up to f=2 kHz.

4.1.3. Far-field noise

The PSD of the LE far-field noise spectrum of each airfoil for $U_\infty \approx \{15, 20, 25, 25, 30, 35, 40\}$ m/s is shown in Figs. 9, 10, 11, and 12 (a) in narrowband. Note that the inflow velocity was kept constant among the airfoils but the Reynolds number changes depending on the airfoil chord. The hump observed in the low-frequency (≈250 Hz) for the higher velocities is caused by the rod vortex shedding. The hump also appears for lower velocities, however, that part of the spectrum is not shown here because of the contamination of the background noise. Figs. 9, 10, 11, and 12 (b) show the LE noise scaled with the inflow turbulence characteristics, as proposed by Glegg and Devenport [56]. Note that, assuming that u_{rms} is linear to the inflow velocity, the LE noise level scales with a power of 3 with the inflow velocity when the frequency is also normalized using the inflow velocity. The scaling shows a good overlap of the noise curves for each airfoil, i.e., within 4 dB for St_c(= fc/U)<5 and within 1 dB for St_c>5. The case of U_∞≈15 m/s presents the worst scaling for all the airfoils, most probably because of the higher background noise contamination at this lower velocity.

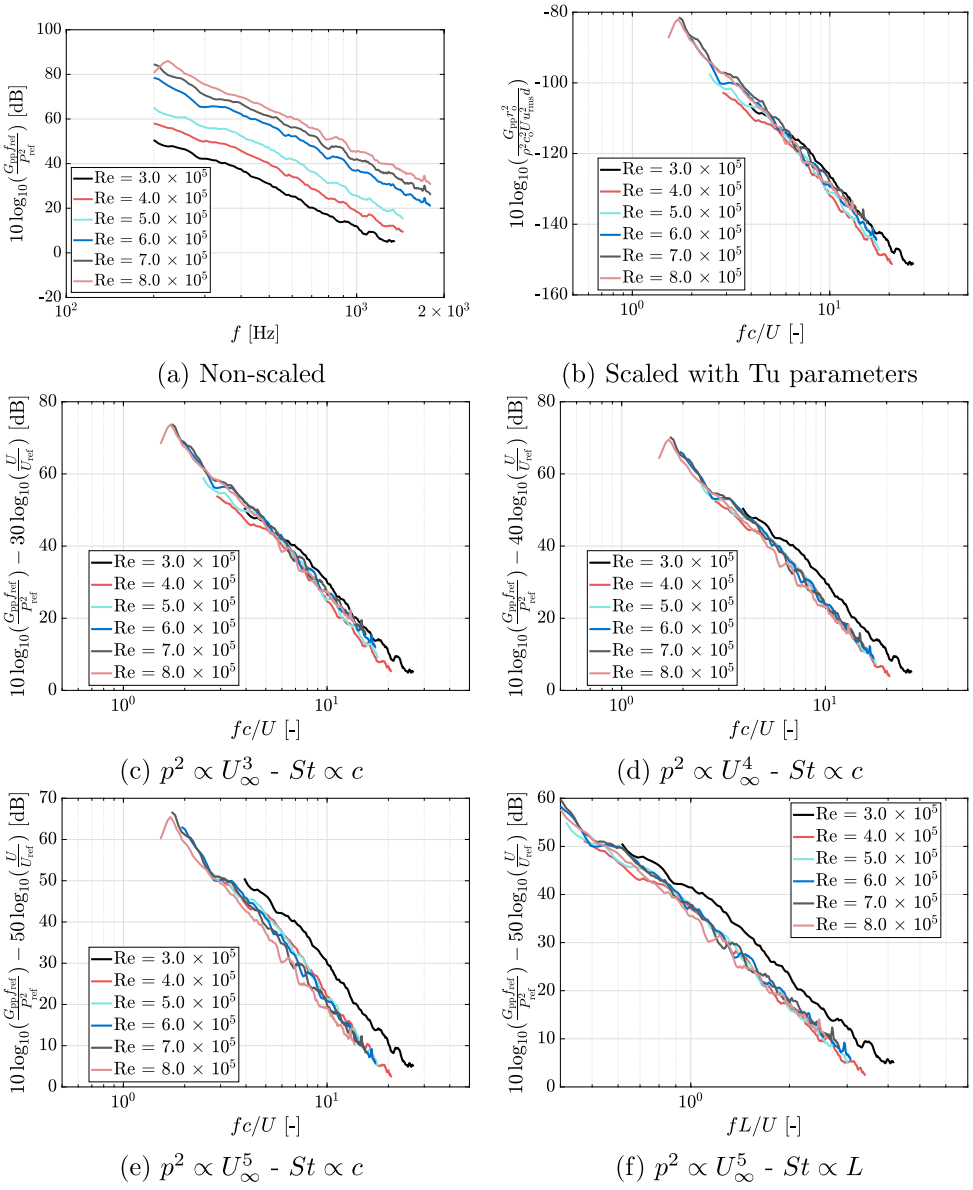

Fig. 12. LE noise for several Reynolds numbers of NACA 63018 airfoil.

Figs. 9, 10, 11, and 12 (c,d,e) show the LE noise scaled with the velocity using a power of 3, 4, and 5, respectively, with the frequency scaled to a Strouhal number based on to the airfoil chord and inflow velocity (St_c). The reference velocity is the lowest velocity, i.e., U_{ref}=15 m/s. The LE noise scales with the power of 5 of the inflow velocity for the low-frequency range, and the best scaling is shifted towards the power of 3 for higher frequencies, see Figs. 9 to 12 (c,d,e), which would correspond to integrated energy levels scaling with the powers 6 and 4 of the incoming flow speed, respectively [65]. This behavior is explained by the acoustic compactness of the airfoil. For low frequencies, the airfoil acts as a single dipole, showing a scale of 6 with the velocity. As the frequency increases and the airfoil becomes a non-compact noise source, the scattering of the noise produced by the presence of the TE reduces the scaling of the far-field noise with the inflow velocity to a power of 4. The NACA 0018 and 0012 become a non-compact noise source at f=270 Hz, whereas the NACA 0008 and 63018 become a non-compact noise source at f=180 Hz, corresponding to St_c=2.7 for all the airfoils, based on U_∞=30 m/s and each airfoil's chord. The results show that the LE noise scale is better with the power of 5 up to $St\approx3$, where the wavelength is comparable with the airfoil chord, with the power of 4 for 2.5<St<6, and with the power of 3 for St>6, which would correspond to integrated energy levels scaling with the powers 6, 5, and 4 of the incoming flow speed, respectively [65]. Despite the analysis at lower frequencies (St<2.6) being limited due to the cut-off frequency of the anechoic chamber and the near-field effects on the microphones, a clear tendency of the reduction in the scaling factor with the inflow velocity for higher frequencies is observed, which is most probably due to the non-compactness of the airfoil.

Figs. 9 to 12 (f) show the scaling of LE noise with the power of 5 of the velocity using the turbulent integral length scale (L) and inflow velocity (U_∞) to normalize the frequency ($St_L = fL/U$). The scaling with the power of 5 is better when the frequency is normalized using L than when normalized using c, mainly for higher inflow velocities. For the NACA 0018 and 0012, the far-field noise spectra collapse within 3 dB for $Re \geq 5\times10^5$ in the entire frequency range (see Figs. 9 and 10 (f)). For the NACA 0008, the far-field noise spectra collapse within 2 dB for $Re\geq4\times10^5$ and $St_L\leq3$ (see Fig. 11 (f)). For the NACA 63018, the far-field noise spectra collapse within less than 1 dB for $Re \geq 4\times10^5$ in the entire frequency range (see. Fig. 12 (f)). This shows a clear tendency

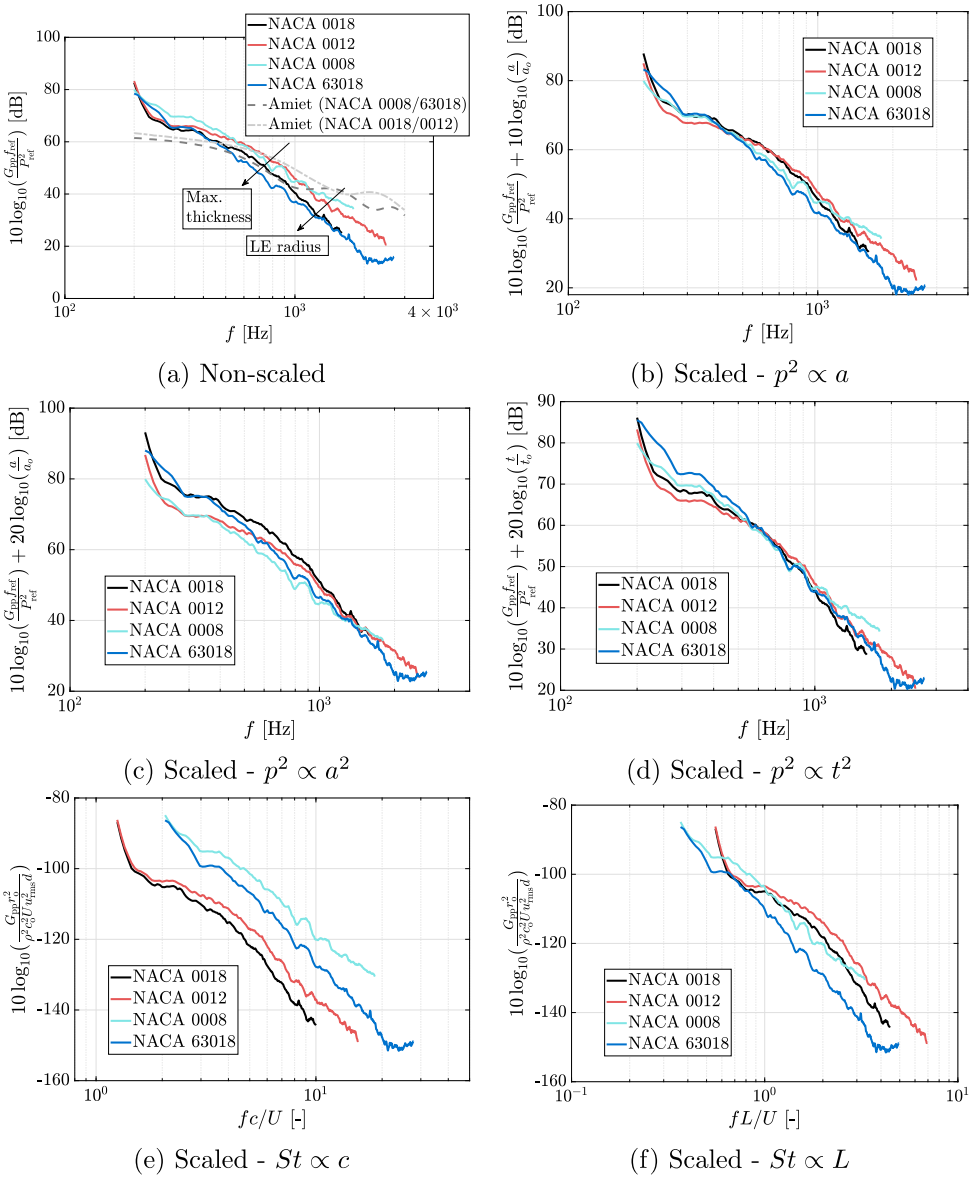

Fig. 13. LE noise of several airfoils. U_∞=30 m/s. Re=4×10^5 for the NACA 00018 and 00012, and Re=6×10^5 for the NACA 0008 and 63018.

of a better scaling for higher Reynolds numbers for all the airfoils. According to Table 3, the length scale varies with the velocity. Therefore, in the normalization of the frequency using L, the velocity is implicitly considered. Linear and quadratic functions adjust the variation of L as a function of U_∞ with similar adjustment coefficients for both turbulence. Therefore, we cannot conclude whether $L \propto U_\infty$ or $L \propto U_\infty^2$. However, we can conclude that considering a scaling of U^5 with L normalizing the frequency, we actually have a scaling of the integrated energy levels with powers of 5 or 4 of the incoming flow speed, which is similar to what is obtained when c is used to normalize the frequency.

Fig. 13(a) shows the LE far-field noise produced by the several airfoils at $U_\infty \approx$30 m/s. As Amiet's theory only considers the inflow turbulence conditions for the noise prediction, only two curves with the noise prediction are shown; one for each pair of airfoils submitted exactly to the same inflow conditions with the same chord. For $f \leq$1 kHz, Amiet's theory well predicts the decay of the far-field noise spectrum level as a function of the frequency. However, for higher frequencies, the experimental spectra show a stronger decay of the G_{pp} as a function of the frequency, and Amiet's method significantly deviates from the experimental results, over-predicting the far-field noise. As a general observation, the LE reduces as the maximum thickness (t) and LE radius (a) increase. Similar results have been found in the literature [39,41]. However, the effect of t and a on the LE far-field noise depends on the frequency range, which has not been directly addressed in the literature. Similar noise levels were obtained for the NACA 63018 and NACA 0018 in the low- and high-frequency ranges, whereas in the mid-frequency range, i.e., 0.5<f<1.5 kHz, the NACA 0018 produces higher noise. Note that those airfoils have the same t/c ratio and similar a, but the absolute thickness of each airfoil is different. Contrarily, the NACA 0012 and 0008 airfoils, which have different t/c ratio and a but the same absolute thickness, produce similar noise levels in the mid-frequency range (0.5<f<1.2 kHz) and the NACA 0008 is louder in the low- and high-frequency ranges. This demonstrates that the airfoil absolute thickness is more relevant in the mid-frequency range, whereas the LE radius is more relevant in the high-frequency range. As the leading-edge radius is smaller than the airfoil thickness, it affects mainly the higher frequencies. Therefore, one could expect the LE noise scales with those parameters for the frequency ranges where they have more influence. Fig. 13(b, c, d) show the LE noise level of the several airfoils scaled with a power of 1 of the LE radius, a power of 2 of the LE radius, and a power of 2 of the maximum airfoil thickness, using the geometrical characteristics of the NACA 0008 as reference. From the results, we

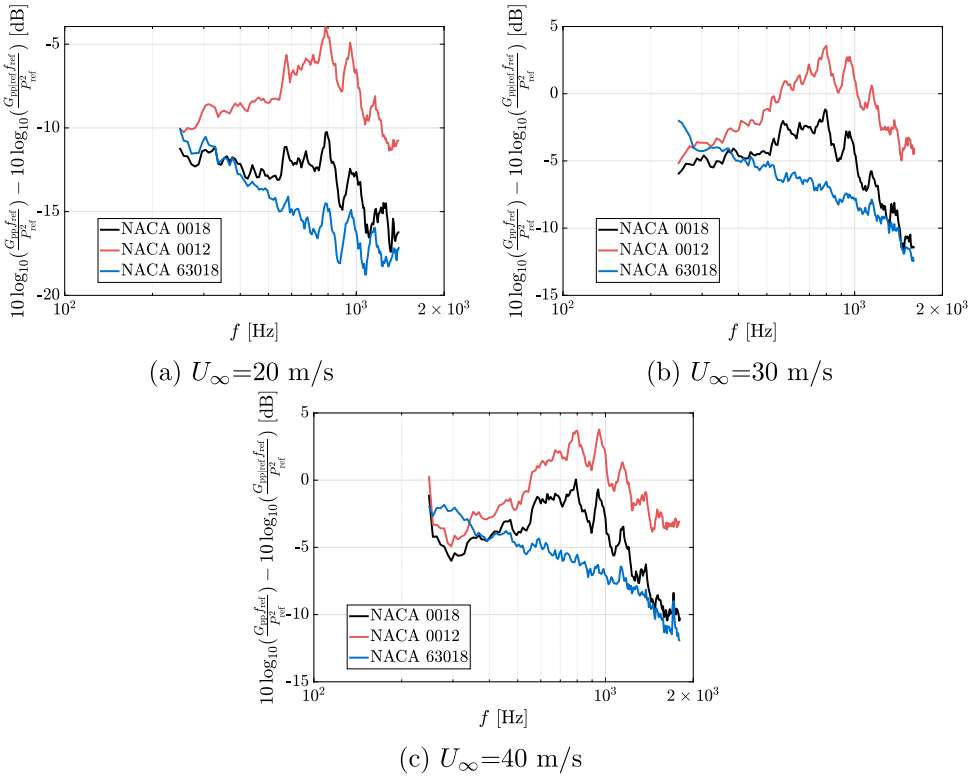

Fig. 14. Relative level of the LE noise with respect the NACA 0008 airfoil for several inflow velocities.

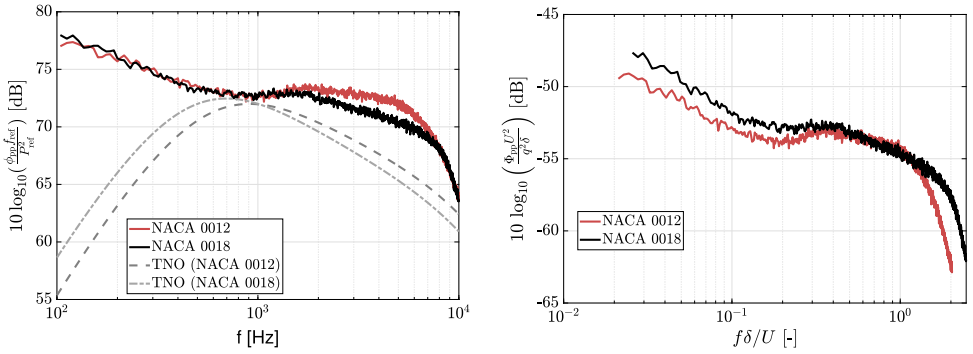

Fig. 15. Wall-pressure spectrum of NACA 0012 and NACA 0018 airfoils. U_∞=30 m/s. Re=4×10^5.

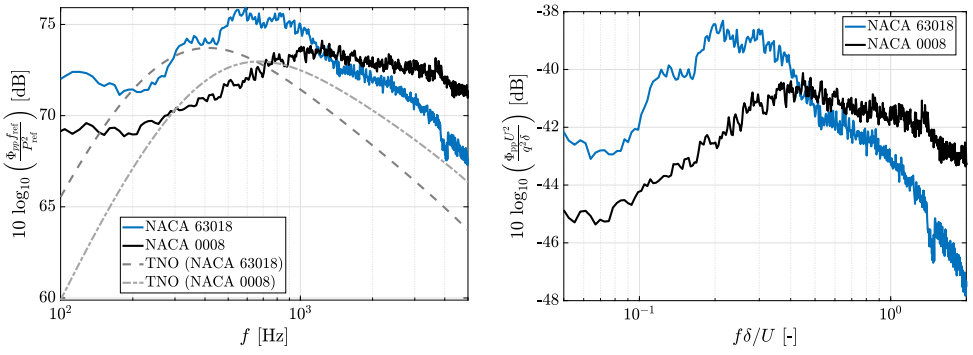

Fig. 16. Wall-pressure spectrum of NACA 0008 and NACA 63018 airfoils. U_∞=30 m/s. Re=6×10^5.

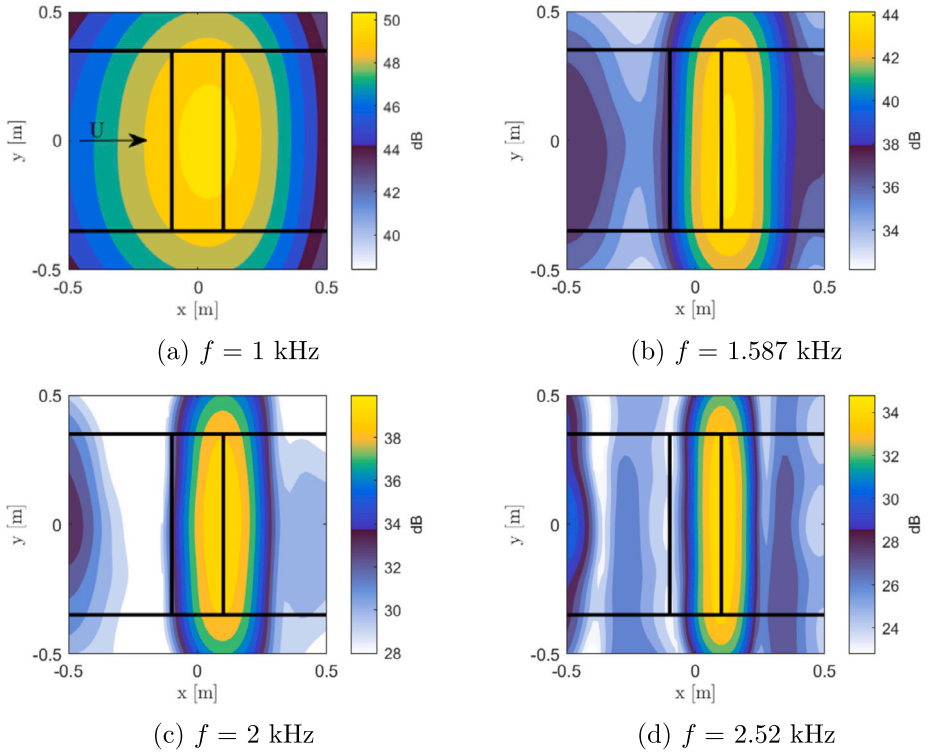

Fig. 17. Beamforming maps without inflow turbulence for NACA 0018 airfoil. U_∞=30 m/s.

can conclude that: I. For f<0.5 kHz, the far-field noise spectra collapse within 3 dB when scaled with the power of 1 of a. Similar results were found when using t. Those results are not shown here for simplicity. II. For 0.5<f<1.2 kHz, the far-field noise spectra collapse within less than 1 dB when scaled with a power of 2 of t. III. For 1.2<f<1.8 kHz, the far-field noise spectra collapse within 1 dB when scaled with a power of 2 of a. These scaling factors are the first step to modeling the effect of the airfoil geometry in the LE noise prediction.

Fig. 13(e) shows the LE noise produced by several airfoils scaled by inflow turbulence parameters and the Strouhal number based on the airfoil chord. The noise of the several airfoils do not scale with the inflow turbulence parameters, even for the exact same inflow turbulence conditions. The frequency scaling is significantly improved when the integral turbulent length scale is used for the calculation of the Strouhal number, see Fig. 13(f). However, the LE noise level still does not scale with the inflow turbulence parameters. This shows that the scaling based on the inflow turbulent conditions is valid for a single geometry but it is not relevant when comparing several geometries, indicating a great influence of the airfoil geometry on the noise production and the necessity of incorporating the geometry in LE noise prediction methods.

Fig. 14 shows the relative level of the NACA 0018, 0012, and 63018 with respect to the NACA 0008 airfoil for several inflow velocities. As observed before, the noise is reduced by the airfoil thickness. This reduction is more significant for higher frequencies, as also observed by [39–41]. However, the results show that the geometry effects are reduced with the inflow velocity, oppositely of what was observed by Gill et al. [41].

4.2. Trailing-edge noise

4.2.1. Wall-pressure spectrum

This section compares the measured wall-pressure spectrum of the different airfoils with the TNO-Blake model. Due to the different measurement techniques used and different locations of the microphones, only the NACA 0018 and 0012 are compared between them, and separately, the NACA 0008 and 63018 are compared between them to ensure that the differences in the wall-pressure spectra are caused by the airfoil geometry. Fig. 15(a) shows the wall-pressure spectrum for the NACA 0018 and 0012. The NACA 0012 has a higher level of the wall-pressure spectrum for 1.8<f<8 kHz, which is reflected in the higher far-field noise in this same frequency range, see Fig. 22(a). Fig. 15(b) shows the wall-pressure spectrum scaled with the boundary layer parameters. The wall-pressure spectra collapse with less than 1 dB in the Strouhal number range of 0.4 to 1.5. Fig. 16 shows the dimensional wall-pressure spectrum for the NACA 0008 and 63018 (Fig. 16(a)) and normalized with the boundary layer parameters (Fig. 16(b)). The wall-pressure spectra of the NACA 0008 and 63018 do not scale with the boundary layer parameters. The NACA 63018 presents the maximum level along the frequency range at a lower frequency than the NACA 0008, which is expected because of the thicker boundary layer of the NACA 63018. For f>1.2 kHz, the wall-pressure spectrum level of the NACA 0008 is higher than the NACA 63018. For all the airfoils, the TNO-Blake model under-predicts the level of the wall-pressure spectrum mainly in the high-frequency range. However, it well predicts the relative level of the wall-pressure spectrum between the airfoils along the frequency range. We used TNO-Blake model in this research since it presents a better wall-pressure spectrum prediction in a wider range of applications compared to the empirical methods that are available in the literature that are very sensitive to the boundary layer inputs. Despite it being a method based on physical principles, the obtention of the flow quantities across the boundary layer is through semiempirical relationships. Therefore, the poor agreement between the TNO-Blake model and the experimental results might be attributed to the empirical relationships. The wall-pressure spectrum was also predicted using experimental measurements of the boundary layer instead of the results from XFOIL; however, a difference of less than 1 dB is obtained in the entire frequency range. This analysis is not shown here for conciseness.

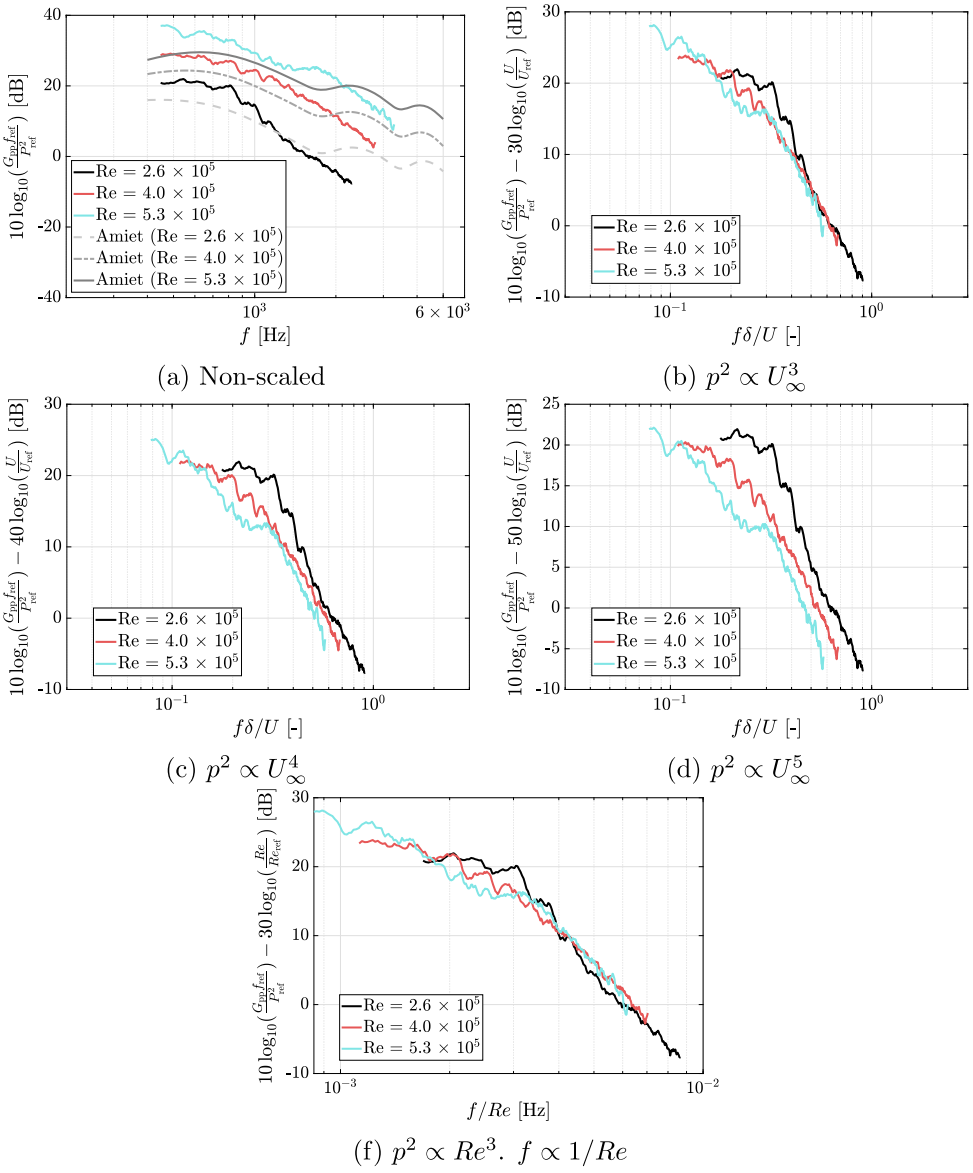

Fig. 18. TE noise for several Reynolds numbers of NACA 0018 airfoil.

4.2.2. *Beamforming maps*

Fig. 17 shows the one-third octave beamforming maps for several central frequencies for the NACA 0018 at U_∞=30 m/s. The beamforming maps for other airfoils are shown in Figs. A.25, A.26, A.27 in Appendix A. For all airfoils, for f>1 kHz, a well-defined noise source at the TE distributed along the span is observed. No spurious noise sources are observed.

4.2.3. *Far-field noise*

Figs. 18, 19, 20, and 21 show the TE far-field noise spectra in narrowband of each airfoil compared with Amiet's theory for $U_\infty = \{20, 30, 40\}$ m/s. For airfoils NACA 0008, and 63018 the measured wall-pressure spectrum (Φ_{pp}^m) was also used as input in Amiet's model for U_∞=30 m/s to analyze the prediction method isolating the accuracy of the wall-pressure spectrum method, see Figs. 20 and 21. Analyzing the cases of the measured wall-pressure spectrum used as input, it is noted that Amiet's method under-predicts the noise in the low-frequency range and over-predicts the noise in the high-frequency range. The poor agreement in the low-frequency range between Amiet's theory and experimental measurements could also be related to the lower performance of the microphone array for lower frequencies. As the TNO-Blake model under-predicts the wall-pressure spectrum in the high-frequency range, a better agreement with the measured far-field noise is obtained using the TNO-Blake wall-pressure spectrum as input in Amiet's theory. In general, Amiet's model coupled with the TNO-Blake model presents a good agreement with experimental measurements in the mid-frequency range. Such a range is shifted towards higher frequencies for higher velocities. Furthermore, a better agreement between Amiet's theory and the experiments is obtained for the NACA 0008 due to its higher similarity with a flat plate. Contrary, the poorest agreement is obtained for the NACA 63018 due to its thickness, which can be also related to the changing of the directivity pattern for thick airfoils.

Figs. 18, 19, 20, and 21(b,c,d) show the TE noise for each airfoil scaled with the inflow velocity with the powers of 3, 4, and 5. The frequency is normalized using the boundary layer thickness at the airfoil TE and the inflow velocity. For all cases, the best scaling of the TE noise is with the power of 3 with the inflow velocity in the entire frequency range. Following the discussion of the acoustic compactness of the airfoil addressed in Sec. 4.1.3, in the frequency range where the TE noise is produced in the cases presented in this study (1<f<4 kHz), the airfoil is a non-compact noise source. Hence, the scattering effects of the LE cause the velocity scaling to be reduced to a power of 3, which

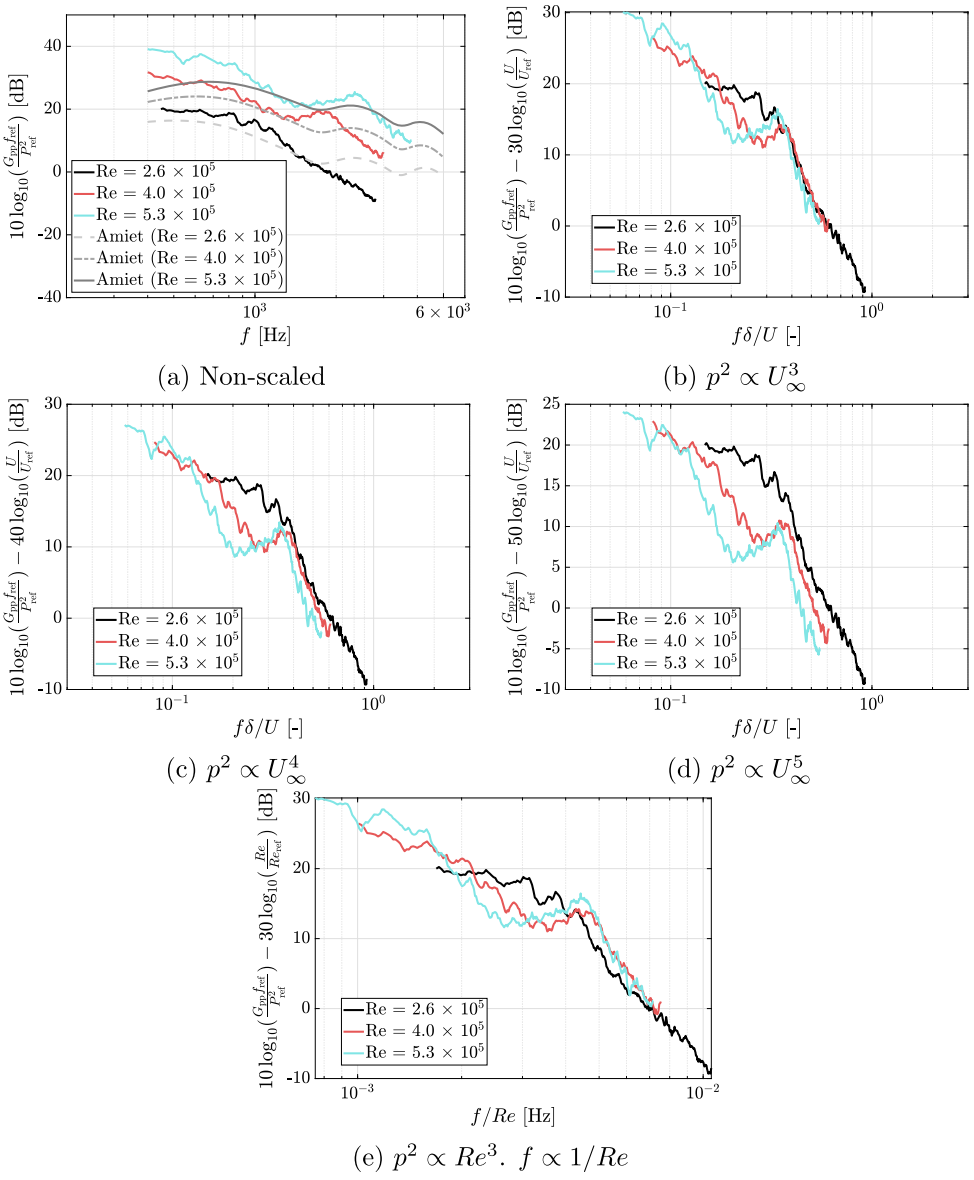

Fig. 19. TE noise for several Reynolds numbers of NACA 0012 airfoil.

means a scaling of the integrated energy levels with a power of 4 of the inflow velocity. Note that the boundary layer thickness also implicitly considers the velocity, which also changes the velocity scaling.

Figs. 18, 19, 20, and 21(e) show the TE noise of each airfoil scaled using the Reynolds number. The frequency of the TE noise scales inversely to the Reynolds number, whereas the spectrum level scales with a power of 3 of the Reynolds number. For the airfoils NACA 0018, 0008, and 63018, the far-field noise spectra collapse within 2 dB in the entire frequency range when using the scaling based on the Reynolds number. For the NACA 0012 the scaling is not as good as for the other airfoils since this airfoil presents blunt TE noise for higher Reynolds numbers that is not observed for $Re = 2.6 \times 10^5$. When analyzing a single airfoil, the Reynolds number only considers the effect of the inflow velocity. Therefore, this scaling is equivalent to the power of 3 with the inflow velocity. However, this scaling remains valid when several geometries are used. This will be further analyzed later in this section.

A hump in the high-frequency range is observed for some cases: The NACA 0018 shows a hump for Re=40×10^5 at $f\delta/U$=0.3, see Fig. 18(b); the NACA 0012 shows a hump for $Re \geq 40 \times 10^5$ at $f\delta/U$=0.35, see Fig. 19(b); and The NACA 0008 shows a hump for all Reynolds numbers at $f\delta/U = 0.7$; see Fig. 20(b). It is caused by blunt trailing edge noise, which occurs when the TE thickness is thick compared to the boundary layer at the TE. Therefore, this noise source is more relevant for higher velocities. However, there is no final agreement about at which conditions it should appear [66,24]. The hump scales with a power of 3 with the inflow velocity. Previous research has found a Strouhal number for blunt TE noise ($St_{t_{TE}} = f t_{TE}/U$) between 0.08 and 0.11, using as characteristic length the TE thickness (t_{TE}) [67–69]. For the NACA 0018, 0012, and 0008 used in this research $St_{t_{TE}}$ ranged from 0.085 to 0.97 considering all the velocities for the three airfoils. $t_{TE} = 0.002$ m for the NACA 0018 and 0012 and $t_{TE} = 0.001$ m for the NACA 0008 and 63018. The NACA 63018 does not show blunt TE noise for any velocity since it has a thicker boundary layer.

Fig. 22(a) shows the TE noise of all the airfoils at the same inflow velocity. No clear tendency about which airfoil produces a louder noise along the frequency range is observed. We would expect that the NACA 0018 and 63018 would produce louder noise in the low-frequency range since they have a thicker boundary layer, which is observed for 0.7<f<1.5 kHz. For f>1.5 kHz, the NACA 63018 produces a significantly louder noise than NACA 0018, i.e., more than 8 dB.

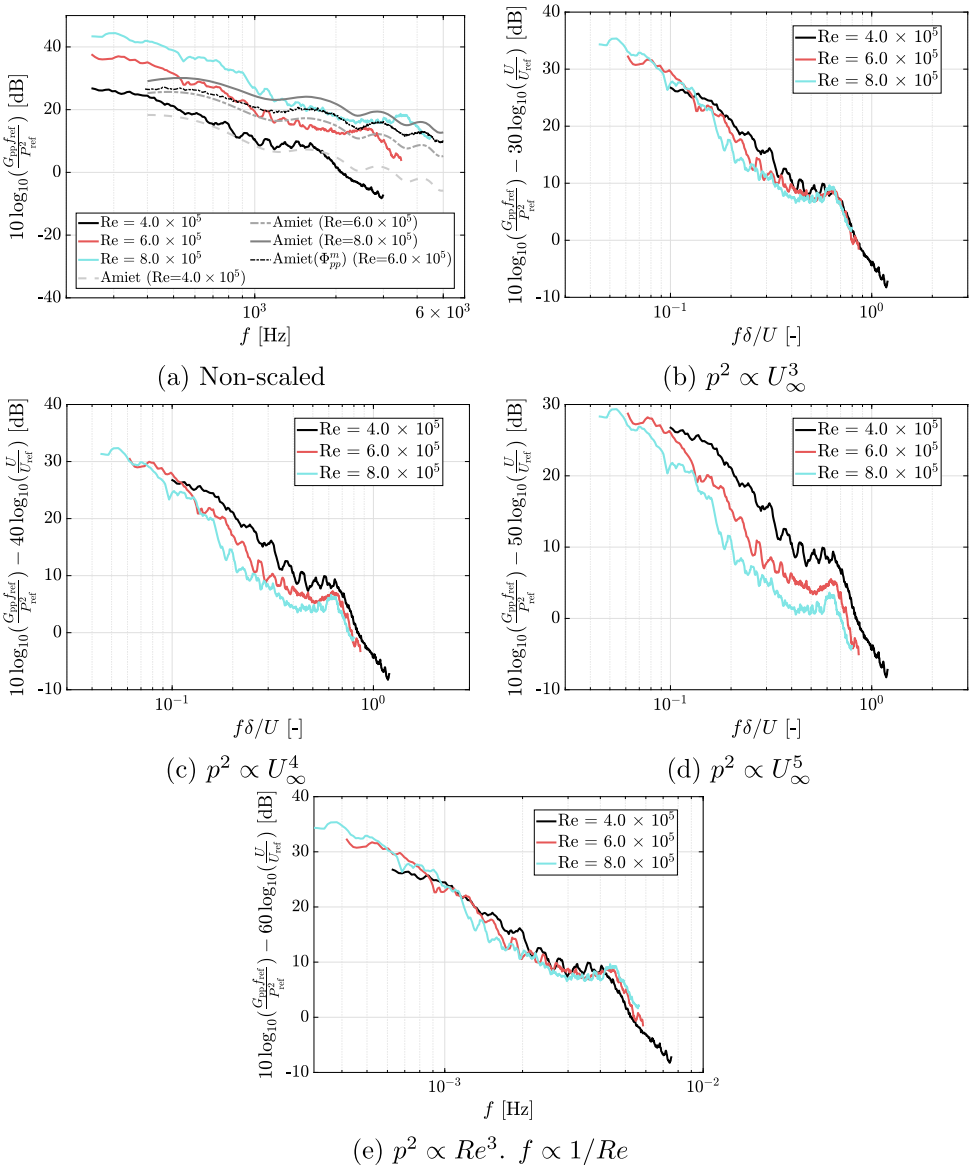

Fig. 20. TE noise for several Reynolds numbers of NACA 0008 airfoil.

The NACA 0008 produces the lowest noise up to f=2 kHz. Above this frequency, the blunt TE noise is higher than the TE noise of the other airfoils.

As observed for every single airfoil, the frequency of the TE noise scales with the inverse Reynolds number and the level scales with a power of 3 of the Reynolds number, see Fig. 22(b). With this scaling, the TE far-field noise spectra collapse within 2 dB in a frequency range from 0.6 to 2.8 kHz. It is important to consider that when comparing the different airfoils at the same inflow velocity, the Reynolds number considers only the chord and not the inflow velocity, oppositely to the cases when a single airfoil was analyzed for several inflow velocities.

Fig. 22(c) shows the noise produced by the different airfoils at the same Reynolds number. The noise produced by the NACA 0008 and 63018 is significantly lower than the other airfoils since the velocity is much lower. Of these cases, only the NACA 0012 presents blunt TE noise. As discussed previously, the frequency of the TE noise scales with the Reynolds number. Therefore, for scaling the cases of the same Reynolds number, only a level scaling is needed. Fig. 22(d) shows the scaling of the TE noise spectrum level using a power of 6 of the inflow velocity. The far-field noise spectra collapse within 2 dB in the frequency range from 0.6 to 4 kHz. Note that the scaling for the NACA 0012 is not that good because of the blunt TE noise phenomenon. To further analyze the effect of the inflow velocity and Reynolds number, the TE noise for several Reynolds numbers and inflow velocities is shown in Fig. 22(e). For the Reynolds numbers shown in the figures, the corresponding inflow velocities are: for the NACA 0018 is 30 m/s, for the NACA 0012 is 20 m/s, for the NACA 0008 is 30 m/s, and for the NACA 63018 is 40 m/s. The NACA 0018 and 0012 show similar noise levels among the airfoils because they are submitted to the same inflow velocity. Fig. 22(e) shows the same cases of Fig. 22(d) scaled with a power of 6 of the inflow velocity. The far-field noise spectra collapse within 5 dB in the frequency range from 0.8 to 1.5 kHz, and within less than 1 dB for f>1.5 kHz. Note that the hump for the NACA 0008 is not accounted for in the calculation because it is caused by blunt TE noise. Furthermore, Fig. 22(f) shows the combination of the several scaling discussed, i.e., the frequency inversely proportional to the Reynolds number and the level proportional to the power of 6 of the inflow velocity and power of 3 with the Reynolds number. The far-field noise spectra collapse within 1 dB in the entire frequency range, except

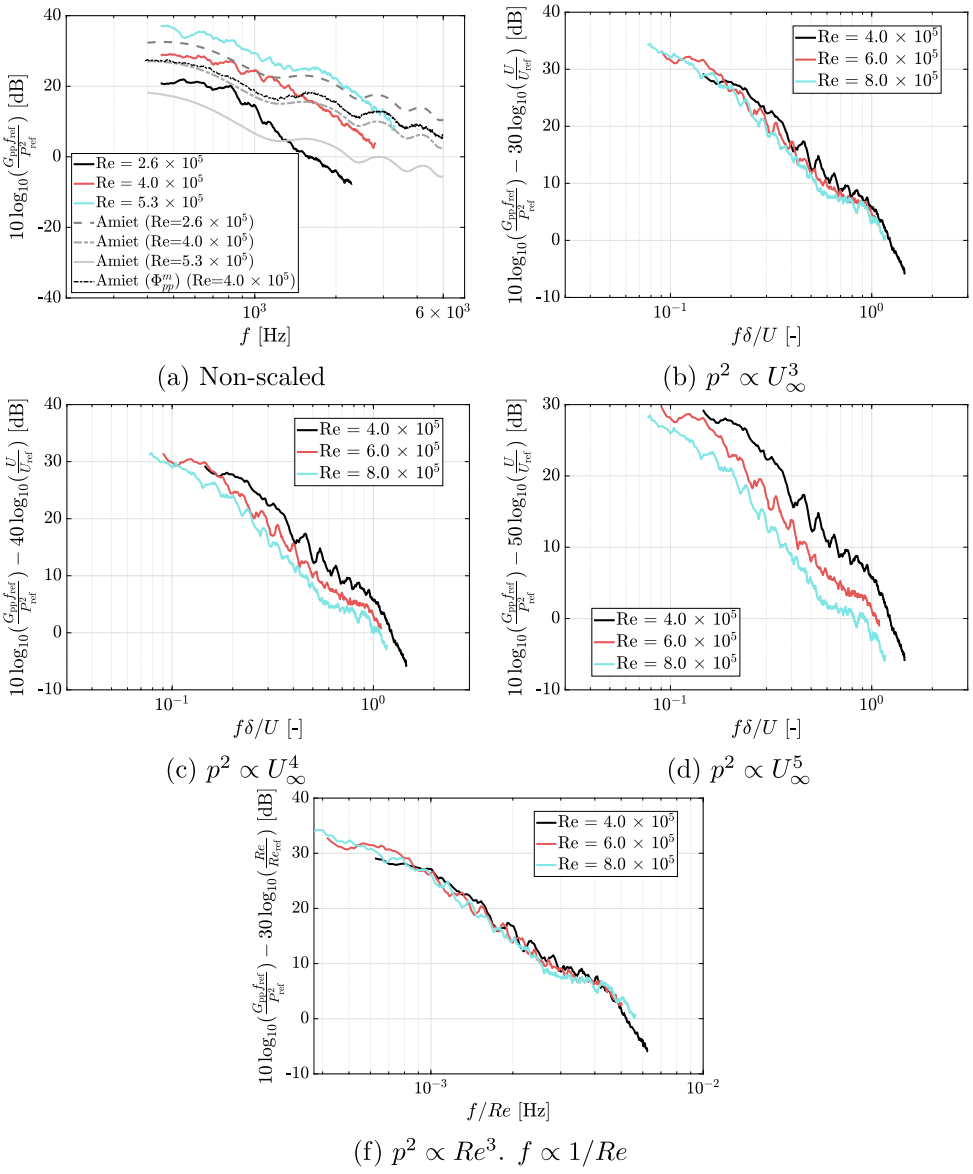

Fig. 21. TE noise for several Reynolds numbers of NACA 63018 airfoil.

for $0.0022<f/Re<0.005$ that collapse within 4 dB. Again, the hump for the NACA 0008 is not accounted for in the calculation since they are caused by blunt TE noise.

5. Competing mechanisms: leading- and trailing-edge noise

The LE and TE noise production highly depends on the airfoil geometry, as discussed throughout the paper. This section aims to compare the noise produced by the NACA 0008 and 63018 when submitted to uniform and turbulent inflows. The noise generation mechanism varies as a function as the frequency and airfoil geometry.

Fig. 23 shows the beamforming maps for the NACA 0008 for the cases with and without inflow turbulence. Note that at f=1 kHz the level-scale of the beamforming contours is not the same for both inflow conditions since with inflow turbulence the noise generated is much higher than the case of uniform inflow (see Figs. 23 (a) and (b)). For $f\geq$2 kHz, the levels of the beamforming contours with and without inflow turbulence are comparable. For the case of uniform inflow at f=1 kHz, the noise source seems to be located at the mid-chord, most probably because of contamination of the beamforming map with the background noise at this specific frequency and low performance of the microphone array (see Fig. 23 (b)). Furthermore, for f≥ 2 kHz the noise source is the TE (see Figs. 23 (d, f, h)). Contrary, for the case of inflow turbulence, the noise source changes along the frequency range. For $f\leq$2 kHz (Figs. 23 (a) and (c)), the noise source is the LE. Note that the LE noise is much higher than the TE noise when the inflow is uniform at a given frequency. At f=2.52 kHz, the case of inflow turbulence shows two noise sources of similar intensity located at the leading and trailing edges (Fig. 23 (e)). The TE noise generated when the inflow is turbulent is higher than the TE noise generated when the inflow is uniform (compare Figs. 23 (e) and (f)). For both inflow conditions at f=3.175 kHz, the beamforming maps show a unique noise source located at the airfoil TE (Fig. 23 (g) and (h)). In the case of inflow turbulence, the beamforming map is more contaminated because of the increase of the background noise with the presence of the rod. However, a noise source at the TE is identified, which is stronger than the case of uniform inflow. The results show that with inflow turbulence the NACA 0008 generates LE noise that dominates the low-frequency range and TE noise that dominates the high-frequency range, which is louder than the noise produced by the airfoil TE with uniform inflow.

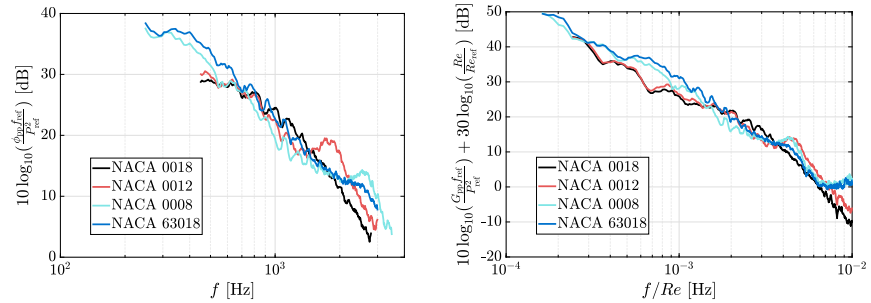

(a) Non-scaled. U_∞=30 m/s (b) Scaled. U_∞=30 m/s

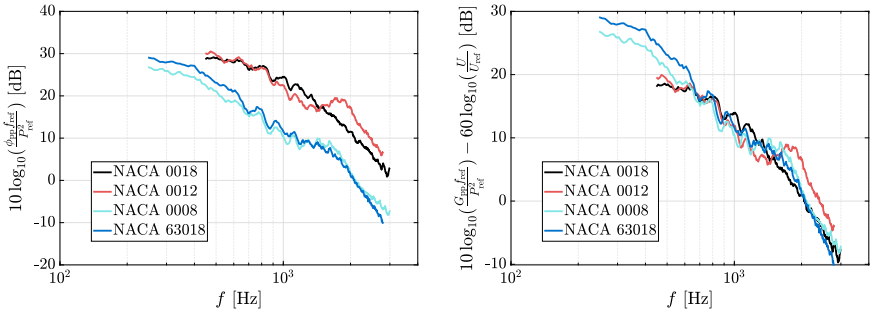

(c) Non-scaled. $Re = 4.0 \times 10^5$ m/s (d) Scaled. $Re = 4.0 \times 10^5$ m/s

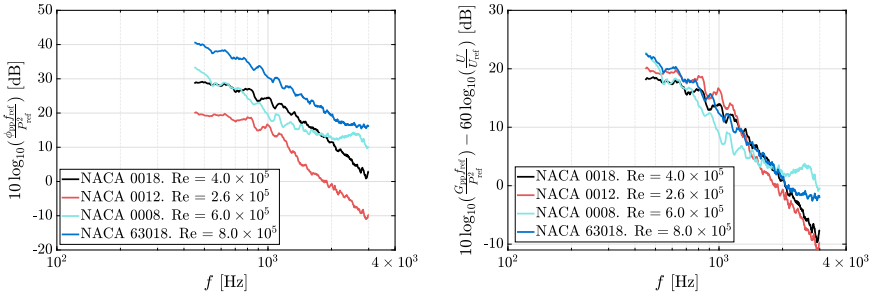

(e) Non-scaled. (d) Scaled. $p^2 \propto U_\infty^6$.

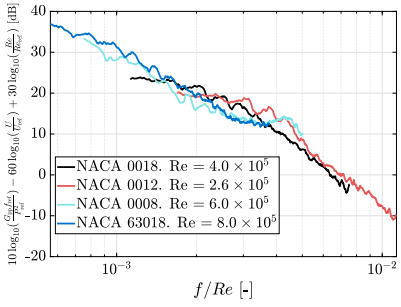

(f) Scaled. $p^2 \propto Re^3 - U^6$. $f \propto 1/Re$

Fig. 22. Trailing-edge noise of several airfoils.

In the mid-frequency range, both mechanisms are similarly important. However, the relative level of the LE and TE noise might vary as a function of the inflow velocity since for U_∞=30 m/s the LE noise is slightly stronger than the TE noise, see Fig. 7(c).

The increase of the TE noise with the inflow turbulence is caused by the penetration of the free-stream turbulence inside the airfoil's boundary layer, which increases the wall-pressure fluctuations at the airfoil TE [70].

Fig. 24 shows the beamforming maps for the NACA 63018 for the cases with and without inflow turbulence. At f=1 kHz, the case with inflow turbulence shows a noise source located at the LE, whereas the case without inflow turbulence shows a noise source located at the airfoil TE (see Figs. 24 (a) and (b)). The noise produced by the LE for the case of inflow turbulence is much stronger than the one produced by the TE for the case without inflow turbulence. For $f \geq 2$ kHz, both inflow conditions show a noise source located at the TE (see Figs. 24 (c-f)). However, the noise produced by the TE in the case with inflow turbulence is much stronger than in the case without inflow turbulence. Note that at f=3.175 kHz the level-scale of the beamforming contour for both cases is not the same since for the case with inflow turbulence the noise produced is much stronger. Furthermore, for the case without inflow turbulence, there is a contamination of the beamforming map in the region of the interaction of the TE with the wind-tunnel bottom wall, showing a noise source at this position (see Fig. 24 (h)).

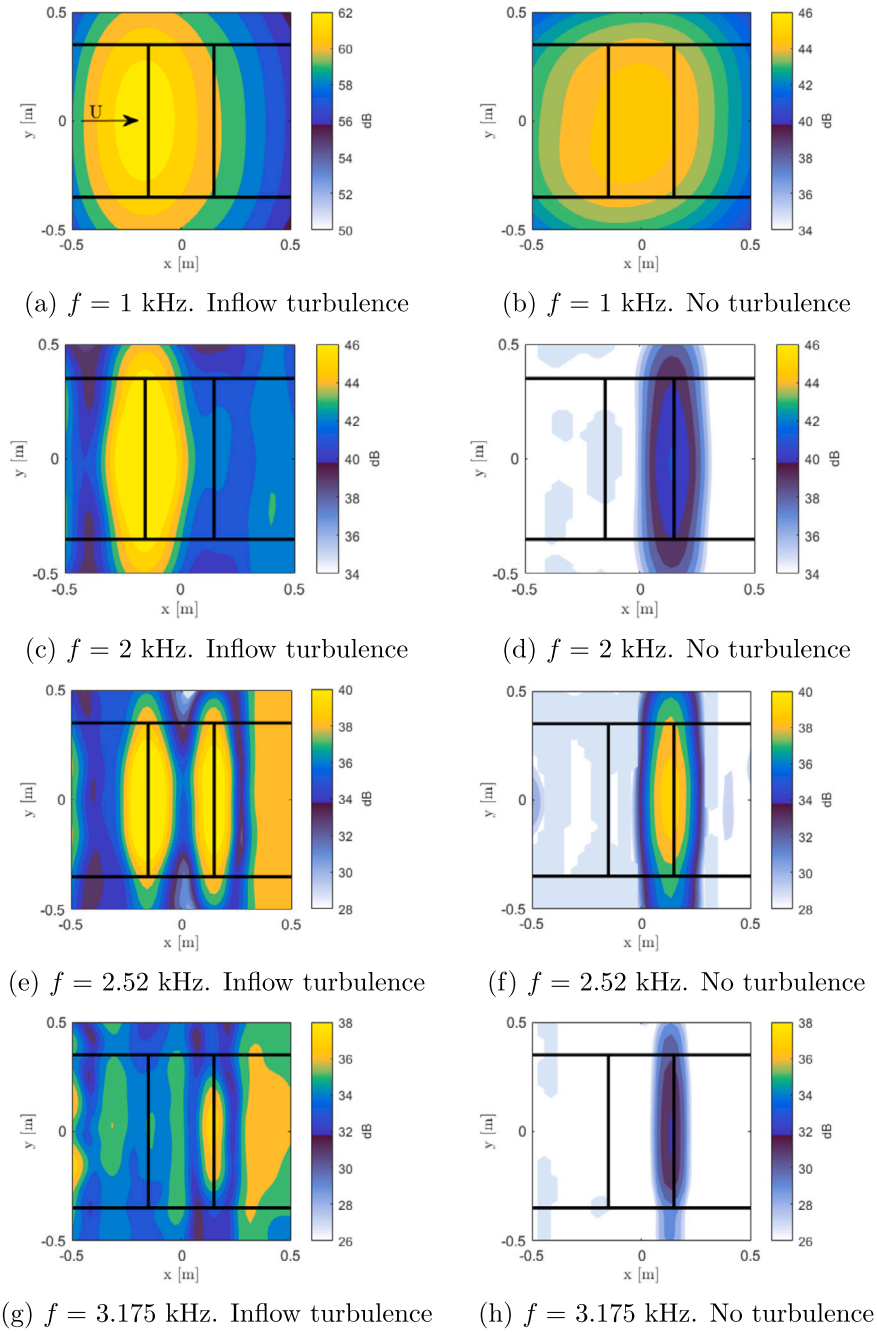

(a) $f = 1$ kHz. Inflow turbulence (b) $f = 1$ kHz. No turbulence

(c) $f = 2$ kHz. Inflow turbulence (d) $f = 2$ kHz. No turbulence

(e) $f = 2.52$ kHz. Inflow turbulence (f) $f = 2.52$ kHz. No turbulence

(g) $f = 3.175$ kHz. Inflow turbulence (h) $f = 3.175$ kHz. No turbulence

Fig. 23. Beamforming maps with and without inflow turbulence for NACA 0008. U_∞=25 m/s.

Different from the NACA 0008, for the NACA 63018 the TE noise dominates almost the entire frequency range for the case with inflow turbulence. This happens because of the combination of two mechanisms: I. the inflow turbulence is more distorted by the thickest airfoil (NACA 63018), which reduces the noise produced by the airfoil LE [71]. II. the free-stream turbulence penetrates inside the boundary layer which increases the airfoil TE noise [70]. The combination of these phenomena is more relevant for thick airfoils, such as the ones used in wind turbines.

For both airfoils, the beamforming maps show that the trailing-edge noise increases. As mentioned before, the increase is due to the penetration of the free-stream turbulence inside the boundary layer. Previous research [70,72] have demonstrated that the free-stream turbulence increases the boundary layer thickness and velocity fluctuations across the boundary layer, which in turn increases the wall-pressure spectrum level close to the airfoil trailing edge, and consequently the trailing-edge noise. For the cases studied in this research, the boundary layer was measured using hot-wire anemometry close to the trailing edge at x/c=0.47 (the same location of the wall-pressure spectrum measurements) with and without inflow turbulence at U_∞=10 m/s for both airfoils and also at U_∞=30 m/s for the NACA 63018.

The inflow turbulence increases the boundary layer thickness from 7.8 mm to 29.3 mm for the NACA 0008, and from 10.2 mm to 23.3 mm for the NACA 63018 at U_∞=10 m/s, and from 8.8 mm to 16.2 mm for the NACA 63018 at U_∞=30 m/s. The large increase in the boundary layer thickness due to the inflow turbulence explains the increase of the trailing-edge noise mainly in the low-frequency range. Further discussion about the free-stream turbulence penetration phenomenon and the impact on the trailing-edge noise is out of the scope of this research.

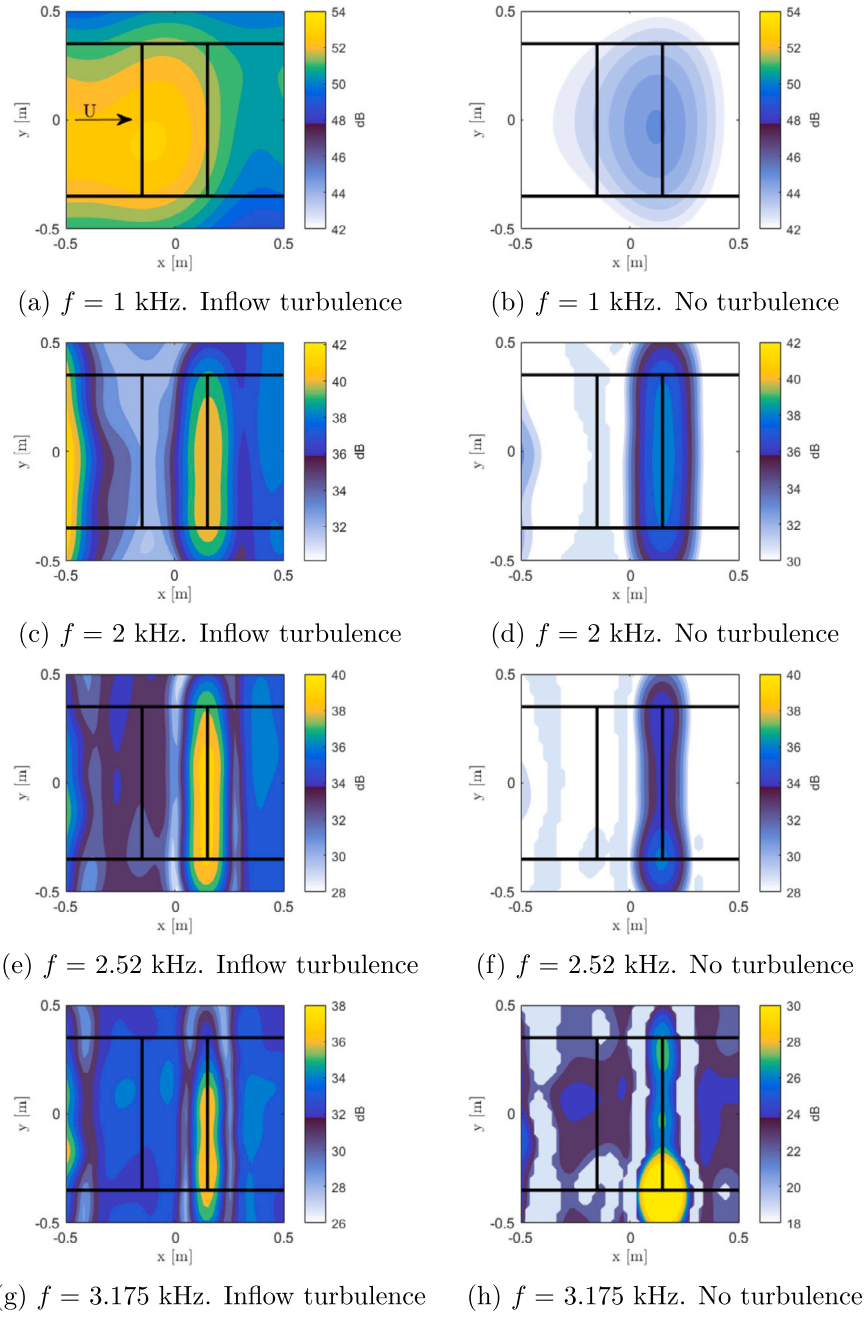

(a) $f = 1$ kHz. Inflow turbulence (b) $f = 1$ kHz. No turbulence

(c) $f = 2$ kHz. Inflow turbulence (d) $f = 2$ kHz. No turbulence

(e) $f = 2.52$ kHz. Inflow turbulence (f) $f = 2.52$ kHz. No turbulence

(g) $f = 3.175$ kHz. Inflow turbulence (h) $f = 3.175$ kHz. No turbulence

Fig. 24. Beamforming maps with and without inflow turbulence for NACA 63018. U_∞=25 m/s.

6. Conclusions

This research presents LE and TE noise measurements, using a microphone phased array, of four different airfoils, i.e., NACA 0018, 0012, 0008, and 63018, which have different chord lengths. The inflow turbulence was generated by a rod located upstream of the airfoils' LE plane. The analyses are composed of the LE and TE far-field noise spectrum of each airfoil for different inflow velocities and a comparison of the LE and TE far-field noise among the airfoils and with Amiet's method. Furthermore, the competition of the LE and TE noise mechanisms when subjected to inflow turbulence is evaluated for the NACA 0008 and 63018.

For the inflow turbulence condition, the beamforming maps showed a noise source located at the LE for the NACA 0008 up to f=2.5 kHz and for the NACA 0012 up to f=1.5 kHz. The NACA 63018 showed a noise source at the TE for frequencies higher than 1 kHz. The airfoil NACA 0018 presented the most contaminated beamforming maps by background noise. For uniform non-turbulent inflow, a localized noise source at the TE is observed for all the airfoils for $f \geq 1$ kHz.

The predicted and experimental LE noise show a good agreement up to $f \approx 1$ kHz. For higher frequencies, the experimental results show a decay of the far-field noise spectrum level as a function of the frequency higher than the predicted. The LE far-field noise scales with a power of 5 with the inflow velocity with the frequency normalized with the airfoil chord and inflow velocity in frequencies where the airfoil is acoustically compact. The scaling is reduced to 3 for high frequencies where the airfoil is non-acoustically compact. The results showed that the LE noise is reduced with the airfoil thickness and LE radius. This reduction increases with the frequency and reduces with the inflow velocity. The airfoil thickness has more influence on the mid-frequency range,

whereas the LE radius has more influence on the high-frequency range. The LE far-field noise level spectrum scales with a power of 1 of the airfoil maximum thickness and LE radius in the low-frequency range, with a power of 2 of the airfoil maximum thickness in the mid-frequency range, and with a power of 2 of the LE radius in the high-frequency range. These scalings serve as a step for modeling the influence of the airfoil geometry on the far-field noise prediction.

The predicted and experimental TE noise show a good agreement in the mid-frequency range. The best agreement is obtained for the thinnest airfoil. Amiet's prediction using the experimental wall-pressure spectrum as input shows that Amiet's method under-predicts the low-frequency range and over-predicts the high-frequency range. The TNO-Blake model significantly under-predicts the high-frequency range of the wall-pressure spectrum. However, it shows a better agreement with the experiments when coupled with Amiet's theory. The TE far-field noise scales with the velocity with a power of 3 in the entire frequency range, with the frequency normalized using the boundary layer thickness and inflow velocity. For a single airfoil at several Reynolds numbers, the frequency scales with the inverse of the Reynolds number, and the far-field noise spectrum level scales with a power of 3 of the Reynolds number. This scaling is still valid when the different airfoils are compared with the same inflow velocity but different Reynolds numbers. Furthermore, TE noise for the different airfoils is compared at the same Reynolds number, and at different Reynolds numbers for each airfoil. For the same Reynolds number, the far-field noise spectrum level scales with a power of 6 of the inflow velocity, whereas for the several Reynolds numbers, the frequency scales with the inverse of the Reynolds number and the level of the far-field noise spectrum scales with a power of 3 of the Reynolds number added to a power of 6 of the inflow velocity. These scalings would also help in future comparisons of TE noise of airfoils at several conditions.

When subjected to inflow turbulence, the NACA 0008 airfoil produces LE noise in the low-frequency range, LE and TE noise of the same intensity in the mid-frequency range, and TE noise in the high-frequency range. Contrary, the NACA 63018 produces LE noise in the low-frequency range up to a frequency much lower than the NACA 0008, and TE noise for higher frequencies. This happens because the thicker airfoil distorts more the inflow turbulence, reducing the LE noise and the frequency range in which it is dominant. The inflow turbulence significantly increases the TE noise compared with the uniform inflow case for both airfoils due to the penetration of the free-stream turbulence inside the boundary layer. The combination of these both phenomena is relevant for wind turbines since thick airfoils are used under high turbulence inflow conditions, making the TE noise source the dominant noise source for a wide frequency range and stronger than the one produced by uniform inflow conditions.

Declaration of competing interest

The authors declare that they have no known competing financial interests or personal relationships that could have appeared to influence the work reported in this paper.

Data availability

Data will be made available on request.

Acknowledgements

The authors would like to acknowledge Ing. W. Lette, ir. E. Leusink, S. Wanrooij for the technical support on the experimental setup and conduction of the experiments. Also, the authors would like to thank Ph.D. M. P. J. Sanders for the insightful discussions during the experimental campaign, for reviewing the manuscript, and for processing the data with the beamforming technique. We would like to thank Msc. A. Bresciani for the guidance in Amiets' theory. Finally, we thank Ph.D. Prof. S. Moreau for the discussions of the results and inputs in the analysis of the data.

Funding Sources

This research received financial support from the European Commission through the H2020-MSCA-ITN-209 project zEPHYR (grant agreement No 860101).

Appendix A. Beamforming maps for uniform inflow

This appendix presents the beamforming maps for uniform inflow at U_∞=30 m/s for the NACA 0012, 0008, and 63018 airfoils.

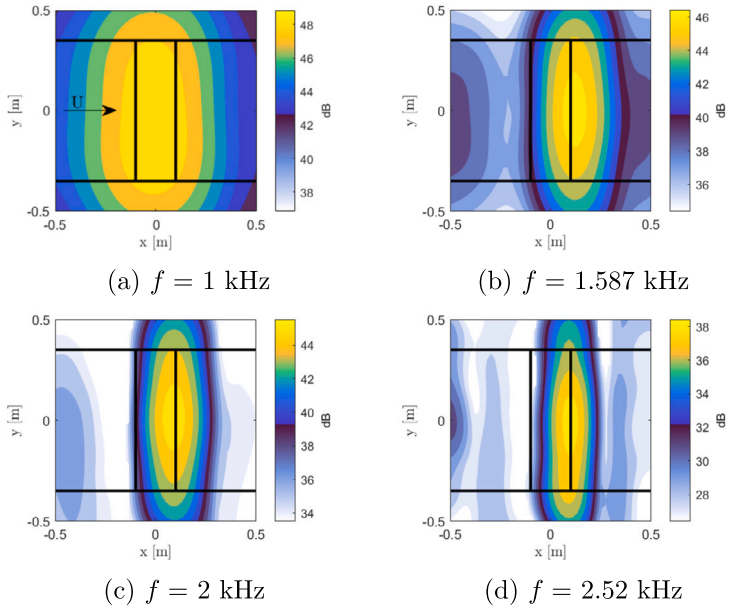

Fig. A.25. Beamforming maps without inflow turbulence for NACA 0012 airfoil. U_∞=30 m/s.

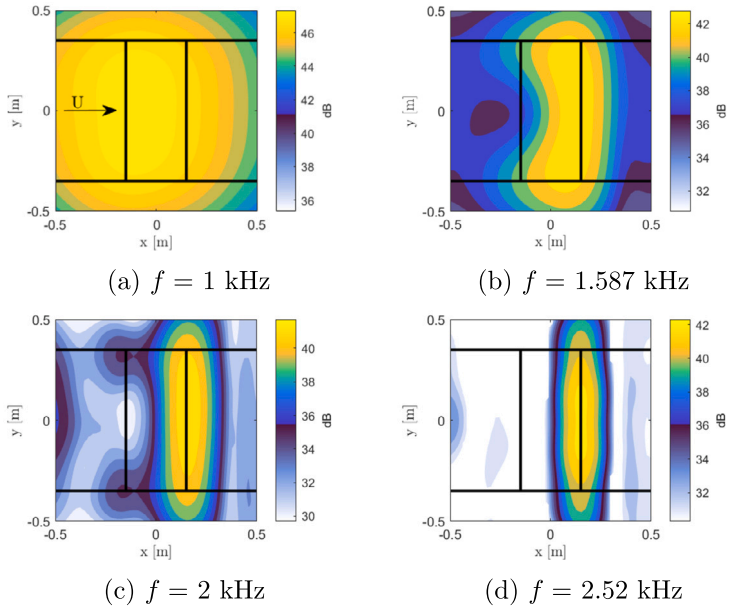

Fig. A.26. Beamforming maps without inflow turbulence for NACA 0008 airfoil. U_∞=30 m/s.

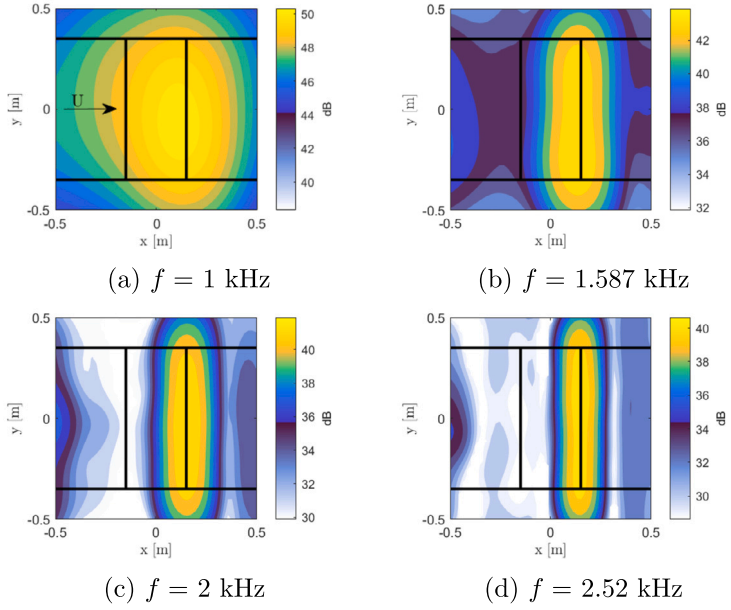

Fig. A.27. Beamforming maps without inflow turbulence for NACA 63018 airfoil. U_∞=30 m/s.

References

[1] Abrahamsen K. The ship as an underwater noise source. Proc Meet Acoust 2012;17(1). https://doi.org/10.1121/1.4772953.

[2] Kurt RE, Khalid H, Turan O, Houben M, Bos J, Helvacioglu IH. Towards human-oriented norms: considering the effects of noise exposure on board ships. Ocean Eng 2016;120:101–7. https://doi.org/10.1016/j.oceaneng.2016.03.049.

[3] Kageyama T, Yano T, Kuwano S, Sueoka S, Tachibana H. Exposure-response relationship of wind turbine noise with self-reported symptoms of sleep and health problems: a nationwide socioacoustic survey in Japan. Noise Health 2016;18(81):53–61. https://doi.org/10.4103/1463-1741.178478.

[4] Götz T, Hastie G, Hatch L, Raustein O, Southall B, Tasker M, et al. Overview of the impacts of anthropogenic underwater sound in the marine environment. Tech. Rep., OSPAR Commission; 2009.

[5] Zwart MC, Dunn JC, McGowan PJ, Whittingham MJ. Wind farm noise suppresses territorial defense behavior in a songbird. Behav Ecol 2015;27(1):101–8. https://doi.org/10.1093/beheco/arv128.

[6] European Parliament. Directive 2002/49/EC of the European Parliament and of the Council of 25 June 2002 relating to the assessment and management of environmental noise. Off J Eur Commun 2002.

[7] ICAO. Environmental report 2016, aviation and climate change 2016; 2016.

[8] Baudin E, Mumm H. Guidelines for regulation on uw noise from commercial shipping. Tech. Rep. Deliverable 5.4. Bureau Veritas, DNV GL; 2015.

[9] Davy JL, Burgemeister K, Hillman D. Wind turbine sound limits: current status and recommendations based on mitigating noise annoyance. Appl Acoust 2018;140:288–95. https://doi.org/10.1016/j.apacoust.2018.06.009.

[10] Abohela I, Hamza N, Dudek S. Effect of roof shape, wind direction, building height and urban configuration on the energy yield and positioning of roof mounted wind turbines. Renew Energy 2013;50:1106–18. https://doi.org/10.1016/j.renene.2012.08.068.

[11] Ricciardelli F, Polimeno S. Some characteristics of the wind flow in the lower urban boundary layer. J Wind Eng Ind Aerodyn 2006;94(11):815–32. https://doi.org/10.1016/j.jweia.2006.06.003.

[12] Carpman N. Turbulence intensity in complex environments and its influence on small wind turbines. Master's thesis. Uppsala University, Disciplinary Domain of Science and Technology, Earth Sciences, Department of Earth Sciences, LUVAL; 2011.

[13] Oerlemans S. Wind turbine noise: primary noise sources. Tech. Rep., National Aerospace Laboratory NLR; 2011.

[14] Amiet RK. Noise due to turbulent flow past a trailing edge. J Sound Vib 1976;47(3):387–93. https://doi.org/10.1016/0022-460X(76)90948-2.

[15] Roger M. On broadband jet–ring interaction noise and aerofoil turbulence-interaction noise predictions. J Fluid Mech 2010;653:337–64. https://doi.org/10.1017/S0022112010000285.

[16] Amiet RK. Acoustic radiation from an airfoil in a turbulent stream. J Sound Vib 1975;41(4):407–20. https://doi.org/10.1016/S0022-460X(75)80105-2.

[17] Sears WR. Some aspects of non-stationary airfoil theory and its practical application. J Aeronaut Sci 1941;8(3):104–8. https://doi.org/10.2514/8.10655.

[18] Chase DM. Modeling the wavevector-frequency spectrum of turbulent boundary layer wall pressure. J Sound Vib 1980;70(1):29–67. https://doi.org/10.1016/0022-460X(80)90553-2.

[19] Goody M. Empirical spectral model of surface pressure fluctuations. AIAA J 2004;42(9):1788–94. https://doi.org/10.2514/1.9433.

[20] Rozenberg Y, Robert G, Moreau S. Wall-pressure spectral model including the adverse pressure gradient effects. AIAA J 2012;50(10):2168–79. https://doi.org/10.2514/1.J051500.

[21] Catlett MR, Anderson JM, Forest JB, Stewart DO. Empirical modeling of pressure spectra in adverse pressure gradient turbulent boundary layers. AIAA J 2016;54(2):569–87. https://doi.org/10.2514/1.J054375.

[22] Kamruzzaman M, Bekiropoulos D, Lutz T, Würz W, Krämer E. A semi-empirical surface pressure spectrum model for airfoil trailing-edge noise prediction. Int J Aeroacoust 2015;14(5–6):833–82. https://doi.org/10.1260/1475-472X.14.5-6.833.

[23] Hu N, Herr M. Characteristics of wall pressure fluctuations for a flat plate turbulent boundary layer with pressure gradients. In: 22nd AIAA/CEAS aeroacoustics conference; 2016. p. 2749.

[24] Blake WK. Mechanics of flow-induced sound and vibration, volume 2: complex flow-structure interactions. Academic Press; 2017.

[25] Parchen RR. Progress report DRAW: a prediction scheme for trailing edge noise based on detailed boundary layer characteristics. TNO Institute of Applied Physics; 1998.

[26] Bertagnolio F, Sørensen N, Johansen J, Fuglsang P. Wind turbine airfoil catalogue. Tech. Rep., Technical University of Denmark; 2001.

[27] Alfredsson PH, Örlü R, Segalini A. A new formulation for the streamwise turbulence intensity distribution. Journal of physics: conference series, vol. 318. IOP Publishing; 2011. p. 022002. https://doi.org/10.1016/j.euromechflu.2012.03.015.

[28] Stalnov O, Chaitanya P, Joseph PF. Towards a non-empirical trailing edge noise prediction model. J Sound Vib 2016;372:50–68. https://doi.org/10.1016/j.jsv.2015.10.011.

[29] von Kármán T. Progress in the statistical theory of turbulence. Proc Natl Acad Sci 1948;34(11):530–9. https://doi.org/10.1073/pnas.34.11.530.

[30] dos Santos FL, Botero-Bolívar L, Venner C, de Santana LD. Modeling the turbulence spectrum dissipation range for leading-edge noise prediction. AIAA J 2022:1–12. https://doi.org/10.2514/1.J061106.

[31] Gruber M. Airfoil noise reduction by edge treatments. Ph.D. thesis. University of Southampton; 2012.

[32] Sanders M, de Santana L, Azarpeyvand M, Venner C. Unsteady surface pressure measurements on trailing edge serrations based on digital mems microphones. In: AIAA/CEAS aeroacoustics conference; 2018.

[33] Herr M, Ewert R, Rautmann C, Kamruzzaman M, Bekiropoulos D, Arina R, et al. Broadband trailing-edge noise predictions—overview of banc-iii results. In: 21st AIAA/CEAS aeroacoustics conference; 2015. p. 2847.

[34] Lee S, Ayton L, Bertagnolio F, Moreau S, Chong TP, Joseph P. Turbulent boundary layer trailing-edge noise: theory, computation, experiment, and application. Prog Aerosp Sci 2021;126:100737. https://doi.org/10.1016/j.paerosci.2021.100737.

[35] Oberai AA, Roknaldin F, Hughes TJ. Computation of trailing-edge noise due to turbulent flow over an airfoil. AIAA J 2002;40(11):2206–16. https://doi.org/10.2514/2.1582.

[36] Oerlemans S, Migliore P. Aeroacoustic wind tunnel tests of wind turbine airfoils. In: 10th AIAA/CEAS aeroacoustics conference; 2004. p. 3042.

[37] Paterson RW, Amiet RK. Noise and surface pressure response of an airfoil to incident turbulence. J Aircr 1977;14(8):729–36. https://doi.org/10.2514/3.58845.

[38] Dean L. Broadband noise generation by airfoils in turbulent flow. In: 5th AIAA/CEAS aeroacoustics conference and exhibit; 1971. p. 587.

[39] Gershfeld J. Leading edge noise from thick foils in turbulent flows. J Acoust Soc Am 2004;116(3):1416–26. https://doi.org/10.1121/1.1780575.

[40] Devenport WJ, Staubs JK, Glegg SA. Sound radiation from real airfoils in turbulence. J Sound Vib 2010;329(17):3470–83. https://doi.org/10.1016/j.jsv.2010.02.022.

[41] Gill J, Zhang X, Joseph P. Symmetric airfoil geometry effects on leading edge noise. J Acoust Soc Am 2013;134(4):2669–80. https://doi.org/10.1121/1.4818769.

[42] Sanders M, Koenjer C, Botero-Bolívar L, dos Santos F, Venner C, de Santana L. Trailing-edge noise comparability in open, closed, and hybrid wind tunnel test sections. AIAA J 2022:1–15. https://doi.org/10.2514/1.J061460.

[43] de Santana LD, Sanders MP, Venner CH, Hoeijmakers HW. The utwente aeroacoustic wind tunnel upgrade. In: 24th AIAA/CEAS aeroacoustics conference; 2018. p. 3136.

[44] Berntsen CR. The remote microphone probe for unsteady surface pressure measurement. Master's thesis. University of Notre Dame; 2014.

[45] Yakhina G. Experimental study of the tonal trailing-edge noise generated by low-Reynolds number airfoils and comparison with numerical simulations. Ph.D. thesis. École Centrale Lyon; 2017.

[46] Botero-Bolívar L, dos Santos FL, Venner C, de Santana LD. Influence of the free-stream turbulence on an airfoil's wall-pressure fluctuations. In: 28th AIAA/CEAS aeroacoustics 2022 conference; 2022. p. 3102.

[47] Sarradj E. Optimal planar microphone array arrangements. In: DAGA 2015; 2015. p. 220–3.

[48] Bahr C, Humphreys W, Ernst D, Ahlefeldt T, Spehr C, Pereira A, et al. A comparison of microphone phased array methods applied to the study of airframe noise in wind tunnel testing. In: 23rd AIAA/CEAS aeroacoustics conference; 2017. p. 3718–36. AIAA 2017-3718.

[49] Sanders M. Aeroacoustic measurements of airframe components: in an open-jet, a hard-wall and a hybrid wind tunnel test section. Ph.D. thesis. University of Twente; 2022.

[50] Brooks T, Humphreys W. Effect of directional array size on the measurement of airframe noise components. In: 5th AIAA aeroacoustics conference; 1999. p. 1958–68. AIAA 99-1958.

[51] dos Santos FL, Botero-Bolívar L, Venner C, de Santana LD. On the turbulence distortion effects for airfoil leading-edge noise prediction. In: 28th AIAA/CEAS aeroacoustics 2022 conference; 2022. p. 3045.

[52] Hinze J. Turbulence. McGraw-Hill; 1972.

[53] Taylor GI. The spectrum of turbulence. Proc R Soc Lond Ser A, Math Phys Sci 1938;164(919):476–90. https://doi.org/10.1098/rspa.1938.0032.

[54] Dos Santos FL, Botero-Bolívar L, Venner C, de Santana LD. Influence of roughness trips on near- and far-field trailing-edge noise. AIAA J 2022;60(10):5880–9. https://doi.org/10.2514/1.J061570.

[55] Bresciani AP, Le Bras S, de Santana LD. Generalization of Amiet's theory for small reduced-frequency and nearly-critical gusts. J Sound Vib 2022;524:116742. https://doi.org/10.1016/j.jsv.2021.116742.

[56] Glegg S, Devenport W. Aeroacoustics of low Mach number flows. Academic Press; 2017.

[57] Roger M, Moreau S. Back-scattering correction and further extensions of Amiet's trailing-edge noise model. Part 1: theory. J Sound Vib 2005;286(3):477–506. https://doi.org/10.1016/j.jsv.2004.10.054.

[58] Drela M. Xfoil: an analysis and design system for low Reynolds number airfoils. In: Low Reynolds number aerodynamics. Springer; 1989. p. 1–12.

[59] dos Santos FL, Botero-Bolívar L, Venner C, de Santana LD. Modeling the turbulence spectrum dissipation range for leading-edge noise prediction. AIAA J 2022:1–12. https://doi.org/10.2514/1.J061106.

[60] Hickling C, Balantrapu NA, Alexander WN, Millican AJ, Devenport WJ, Glegg SA. Turbulence ingestion into a rotor at the rear of an axisymmetric body. In: 25th AIAA/CEAS aeroacoustics conference; 2019.

[61] Morfiadakis E, Glinou G, Koulouvari M. The suitability of the von Karman spectrum for the structure of turbulence in a complex terrain wind farm. J Wind Eng Ind Aerodyn 1996;62(2–3):237–57. https://doi.org/10.1016/S0167-6105(96)00059-1.

[62] Trush A, Pospíšil S, Kozmar H. Comparison of turbulence integral length scale determination methods. WIT Trans Eng Sci 2020;128:113–23. https://doi.org/10.2495/AFM200111.

[63] Moreau S, Roger M. Competing broadband noise mechanisms in low-speed axial fans. AIAA J 2007;45(1):48–57. https://doi.org/10.2514/1.14583.

[64] de Santana L. Semi-analytical methodologies for airfoil noise prediction. Ph.D. thesis. KU Leuven; 2015.

[65] Roger M, Moreau S. Extensions and limitations of analytical airfoil broadband noise models. Int J Aeroacoust 2010;9(3):273–305.

[66] Hansen CH, Doolan CJ, Hansen KL. Wind farm noise: measurement, assessment, and control. John Wiley & Sons; 2017.

[67] Brooks T, Hodgson T. Trailing edge noise prediction from measured surface pressures. J Sound Vib 1981;78(1):69–117. https://doi.org/10.1016/S0022-460X(81)80158-7.

[68] Herr M, Dobrzynski W. Experimental investigations in low-noise trailing edge design. AIAA J 2005;43(6):1167–75. https://doi.org/10.2514/1.11101.

[69] Moreau DJ, Doolan CJ. Noise-reduction mechanism of a flat-plate serrated trailing edge. AIAA J 2013;51(10):2513–22. https://doi.org/10.2514/1.J052436.

[70] Botero-Bolívar L, dos Santos FL, Venner CH, de Santana L. Increase of unsteady pressure at a trailing edge due to inflow turbulence. AIAA J 2022;60(12):6798–813. https://doi.org/10.2514/1.J061719.

[71] Santana LD, Christophe J, Schram C, Desmet W. A rapid distortion theory modified turbulence spectra for semi-analytical airfoil noise prediction. J Sound Vib 2016;383:349–63. https://doi.org/10.1016/j.jsv.2016.07.026.

[72] Botero-Bolivar L, dos Santos FL, Venner C, de Santana LD. Influence of the free-stream turbulence on an airfoil's wall-pressure fluctuations, 28th AIAA/CEAS aeroacoustics 2022 conference. https://doi.org/10.2514/6.2022-3102, 2022.